

Exploring SMEFT operators in the tHq production at the LHC

Monoranjan Guchait and Arnab Roy

*Department of High Energy Physics, Tata Institute of Fundamental Research,
Homi Bhabha Road, Mumbai-400005, India*

E-mail: guchait@tifr.res.in, arnab.roy@tifr.res.in

ABSTRACT: We study the top-quark production along with a Higgs boson and a jet (tHq) at the LHC experiment within the framework of the Standard Model Effective Field Theory (SMEFT). A strategy is developed to constrain the Wilson Coefficients (WC) corresponding to the associated SMEFT operators using the latest LHC measurements. The best-fit values of these WCs are presented. Finally, we demonstrate the feasibility of finding the effects of these operators on various kinematical observables of the tHq process at the LHC. We find that for a set of best-fitted values of the considered WCs, the excess of signal over the backgrounds can be achieved with a reasonable significance at the center of mass energy $\sqrt{s} = 13$ TeV and for integrated luminosity options $\mathcal{L} = 300 \text{ fb}^{-1}$ and 3000 fb^{-1} .

Contents

1	Introduction	1
2	SMEFT operators for tHq	4
3	Constraining operators $\mathcal{O}_{t\phi}, \mathcal{O}_{\phi Q}^{(3)}, \mathcal{O}_{tW}, \mathcal{O}_{Qq}^{(3,1)}, \mathcal{O}_{Qq}^{(3,8)}, \mathcal{O}_{\phi W}$	6
3.1	Cross-section calculation	6
3.2	Experimental measurements	10
3.3	Fisher information matrix	14
3.4	Constraining WCs	16
4	Implications at the LHC	19
4.1	Simulation of events and object selections	21
4.2	Results	23
4.2.1	Effect of SMEFT operators to tHq process	23
4.2.2	Signal and backgrounds	26
5	Summary	29
A	Signal strength in terms of WCs including EFT	32

1 Introduction

Several measurements along with precision tests carried out at LHC experiments, CERN, Geneva, have re-established the theory of interactions among the elementary particles, namely the Standard Model (SM). However, the shortcomings of the SM from the theoretical and as well experimental sides motivate us to think beyond the SM (BSM) physics. Recall, the SM is constructed based on the $SU(3)_c \times SU(2)_L \times U(1)_Y$ gauge symmetry. Therefore, it is natural to expect that the proposed BSM models should be invariant under this gauge group at the electroweak (EW) scale, and respect all measurements that have been done so far in various experiments. Moreover, the lack of evidence of any kind of new physics signal at the current range of energy scale may suggest that the masses of the BSM particles reside at a higher scale or are decoupled from the SM. Intuitively, one can argue that the SM can be thought of as a low-energy manifestation of a more general fundamental description at a very high energy scale, say Λ [1–5]. In this approach, the SM effective theory (SMEFT) is regarded as a useful framework to describe such theories. In recent times, the SMEFT

framework has received a lot of attention and has become a popular choice to study the effect of UV scale physics in a more generalized and comprehensive manner [6, 7].

In the SMEFT prescription, the SM lagrangian is expanded by adding the additional higher order terms [6–8], which can be described as,

$$\mathcal{L}_{\text{SMEFT}} = \mathcal{L}_{\text{SM}} + \frac{1}{\Lambda^2} \sum_{i=1}^{N_{\text{d6}}} C_i^{(6)} \mathcal{O}_i^{(6)}. \quad (1.1)$$

Here \mathcal{L}_{SM} corresponds to the usual SM lagrangian, and the second term represents the EFT part consisting of total N_{d6} number of dimension-6 operators $\mathcal{O}_i^{(6)}$, constructed out of SM fields with coefficients $C_i^{(6)}$ and cut-off scale Λ , preserving $\text{SU}(3)_c \times \text{SU}(2)_L \times \text{U}(1)_Y$ gauge invariance. Here Λ is a dimensionful parameter and C_i 's, which are dimensionless, are known as the Wilson coefficients (WC). In principle, there exist a total of 2499 dimension-6 operators assuming lepton and baryon number conservation, and once the flavor universality is imposed, this number comes down to 59 [7]. Notably, there can be only one SMEFT operator with dimension-5 in this set-up, known as the Weinberg operator, which generates the lepton number violating Majorana mass term for left-handed neutrinos. However, this operator is not relevant to the physics we address in this study.

Obviously, the addition of extra dimension-6 terms in the lagrangian (Eq. 1.1) results in the modification of interactions from its standard form predicted by the SM. Consequently, the contribution due to the SMEFT operators may cause deviations in SM predictions for precision measurements, which in turn constrain the new physics effects and may impose restrictions on the corresponding WCs. It is found that a class of SMEFT operators affects a large variety of known SM processes in a moderate to severe scale [9–33]. Currently, several studies, as reported in the literature, have phenomenologically constrained a larger set of SMEFT operators fitting a combined set of numerous measurements [34–76] carried out at the LHC experiments. Dedicated searches of new physics effects due to SMEFT operators are also carried out widely by the ATLAS and CMS collaborations, and from the non-observation of any excess of events, the excluded ranges of concerned SMEFT operators are predicted [77–98].

In this study, more emphasis is given to explore the feasibility of finding the signature of SMEFT operators at the LHC. As we understand, the inclusion of the SMEFT operators in the SM lagrangian, which is very well tested, may lead to a change in the total as well as in the differential cross-sections. In particular, the interference effects between amplitudes of the SM, and the SMEFT operators may show up very likely at the tail in the differential distributions of cross-sections, of course, depending on the sensitivity of the corresponding set of operators to the given process. Looking for signals of all SMEFT operators together is undoubtedly very complicated, and even may not be feasible at the LHC. Instead, in this study, we consider a different avenue focusing only on a subset of SMEFT operators related to a particular interesting physics process. In this approach, we found that the top quark

production in association with a Higgs boson and a jet,

$$pp \rightarrow tHq, \tag{1.2}$$

is one such interesting choice. This process includes the Yukawa coupling t - t - H which has several significances. For instance, it is the strongest one and a potential source to explore the effects of new physics and the EWSB [99–102]. Already, various precision measurements are carried out at the LHC to test this coupling [89, 103–114]. In addition, the presence of the W - t - b vertex in the above process is also another aspect where the impact of SMEFT operators is known to be significant. The W - t - b vertex can bear the imprints of different UV models [115–121] through the anomalous coupling. Eventually, the combined effects of the SMEFT operators to the t - t - H and W - t - b vertices may lead to some interesting phenomena. For instance, some of the relevant operators lead to energy-growing features in scattering amplitudes [122], resulting in excess in the kinematic distributions of some observables, as we will see at the end. Hence, the prospect of the tHq process in probing this kind of high-scale physics through the SMEFT framework seems to be very promising.

Our study is performed in two steps. Firstly, the set of sensitive SMEFT operators affecting the tHq process is identified. It is realized that the same set of SMEFT operators can also affect some other production processes at the LHC involving top quark in the final state. The deviations of various measurements, such as total and differential cross-sections, signal strengths, asymmetries, etc. from the corresponding theoretical predictions of those processes are used to impose constraints on the associated SMEFT operators. Notably, these SMEFT operators are constrained from global fits also. However, we revisit those constraints only focusing on the most recent measurements sensitive to the chosen set of operators. Secondly, the implications of those constrained operators to various kinematic distributions of the tHq process are investigated. Eventually, we demonstrate the discovery potential of the signatures of SMEFT operators presenting the signal significance observed at the tail of the distributions. We present results for the high luminosity options, $\mathcal{L} = 300 \text{ fb}^{-1}$ and 3000 fb^{-1} , for the LHC experiment with centre of mass energy $\sqrt{s} = 13 \text{ TeV}$. The SMEFT effects on the basic kinematic distributions of the tHq process are studied before [13], but a detailed picture with proper detector simulation, and sensitivity projections at future LHC luminosity options, are found to be absent. Thus, revisiting the tHq production in the SMEFT context, this study points out the importance of this process to single out EFT effects, with detailed simulation and analysis.

This paper is organized as follows. We first identify the number of sensitive SMEFT operators which modify the vertices of the tHq process in section 2. In section 3, considering various measurements at the LHC relevant to these operators, a methodology is developed by which we predict the best-fit values of the corresponding WCs of those operators interesting to us, along with their allowed ranges. Cross sections of the relevant processes are calculated in section 3, including a formulation to construct Fisher information matrix to

correlate the sensitivities of SMEFT operators with them. The effects of those operators in various kinematic distributions of the final state particles of the tHq process are studied in section 4. Finally, in the same section, estimating the contribution of various backgrounds in the signal excess region, we present the signal significances in several kinematic bins. A summary with concluding remarks is presented in section 5.

2 SMEFT operators for tHq

In this section we identify the set of SMEFT operators associated with the process Eq. 1.2. The representative Feynman diagrams at the tree level for the above process are shown in Fig. 1, where the blobs represent the vertices modified by the SMEFT operators.

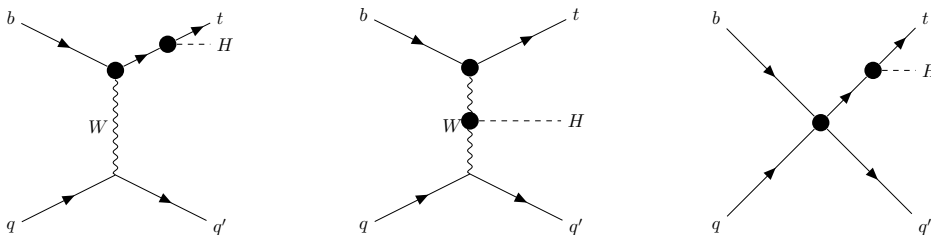


Figure 1: Feynman diagrams of the tHq process in the t-channel.

In this study, we explore the effect of EFT to the t-t-H coupling as well as to the top quark chirality-flipping (W-t-b) interactions through the tHq process. On the other hand, following the standard practice, we neglect the effects of EFTs to the other vertices not involving top-quark ¹. It can be imposed by invoking the symmetry requirement as,

$$U(3)_l \times U(3)_e \times U(2)_Q \times U(2)_u \times U(3)_d \equiv U(2)^2 \times U(3)^3, \quad (2.1)$$

closely following the prescription of the LHC Top Quark Working Group [124], guided by Minimal Flavour Violation (MFV) hypothesis [125]. This assumption is also adopted in the calculations implemented in SMEFTatNLO [126], which we use to compute the cross-sections including EFT effects.

Under this flavor assumption, a larger set of SMEFT operators reduces to seven most relevant operators for the tHq process as shown in Table 1. Here, the Higgs doublet is denoted by ϕ , while $\tilde{\phi} \equiv i\tau^2\phi$; Q and t are the left-handed quark doublet and right-handed singlet respectively; $W_{\mu\nu}^I$ is the $SU(2)_L$ weak gauge field strength tensor and D^μ is the covariant derivative, with $(\phi^\dagger \overleftrightarrow{D}_\mu \phi) \equiv \phi^\dagger (D_\mu \phi) - (\phi^\dagger D_\mu) \phi$. These set of operators modify the couplings, such as W-t-b, t-t-H, and W-W-H involved in the tHq production process as shown in Fig. 1. The point to note here that, these set of operators not only affect the tHq process, but several other important processes involving top-quark and Higgs boson,

¹Effect of EFT to Wqq vertices are expected to be negligible due to strong constraints on the relevant operators from electroweak precision observables (EWPO) [123].

as shown in the last column of Table 1, are also equally affected. All of these processes are studied at the LHC RUN2 experiments by measuring the corresponding cross-sections and other related observables [84, 108, 127–131]. Naturally, any deviation of these measurements from the corresponding SM theoretical predictions including EFT, probably can constrain the WCs of these set of operators. With this intuition, we attempt to find the allowed ranges of the corresponding WCs, consistent with experimental measurements, and eventually predict their best fit values.

Table 1: SMEFT operators contributing to the tHq production (Fig.1) in the Warsaw basis, with an assumption (Eq. 2.1) [124].

Operator	Coefficient	Definition	Coupling	Sensitive processes
$\mathcal{O}_{t\phi}$	$C_{t\phi}$	$(\phi^\dagger\phi - v^2/2)\bar{Q}t\tilde{\phi}$	t- \bar{t} -H	t \bar{t} H, tHq
$\mathcal{O}_{\phi Q}^{(3)}$	$C_{\phi Q}^{(3)}$	$i(\phi^\dagger\overleftrightarrow{D}_\mu\tau_I\phi)\bar{Q}\gamma^\mu\tau^I Q$	W-t-b	tHq, tj, tV, t \bar{t} H
\mathcal{O}_{tW}	C_{tW}	$i(\bar{Q}\sigma^{\mu\nu}\tau_I t)\tilde{\phi}W_{\mu\nu}^I$	W-t-b	tHq, tj, tV, t \bar{t} H
$\mathcal{O}_{Qq}^{(3,1)}$	$C_{Qq}^{(3,1)}$	$(\bar{q}_i\gamma^\mu\tau_I q_i)(\bar{Q}\gamma^\mu\tau^I Q)$	4-Fermion	tHq, tj, t \bar{t} , t \bar{t} H, t \bar{t} V
$\mathcal{O}_{Qq}^{(3,8)}$	$C_{Qq}^{(3,8)}$	$(\bar{q}_i\gamma^\mu\tau_I T_A q_i)(\bar{Q}\gamma^\mu\tau^I T^A Q)$	4-Fermion	tHq, tj, t \bar{t} , t \bar{t} H, t \bar{t} V
$\mathcal{O}_{\phi W}$	$C_{\phi W}$	$(\phi^\dagger\phi - v^2/2)W_{\mu\nu}^I W_I^{\mu\nu}$	H-W-W	tHq, t \bar{t} H
$\mathcal{O}_{\phi D}$	$C_{\phi D}$	$(\phi^\dagger D_\mu\phi)(\phi^\dagger D^\mu\phi)$	H-W-W	tHq, t \bar{t} H

Notice that, among these seven operators, the $\mathcal{O}_{\phi W}$ and $\mathcal{O}_{\phi D}$ mainly affect the Higgs boson coupling with W boson. $\mathcal{O}_{\phi D}$ is expected to be tightly constrained by the measurements of the electroweak precision observables (EWPO) [123]. Therefore, the effects of $\mathcal{O}_{\phi D}$ is not taken into account in our analysis.

The impacts of some of the other relevant SMEFT operators on the decays of the final state particles in the tHq process, in particular, $H \rightarrow b\bar{b}, W^+W^-, ZZ, \tau^+\tau^-, \gamma\gamma$, and $t \rightarrow bW$, are also checked. The WC ($C_{b\phi}$) corresponding to the operator $\mathcal{O}_{b\phi} \equiv (\phi^\dagger\phi)\bar{Q}b\phi$ (though violates the symmetry requirement, Eq. 2.1), modifying the H-b- \bar{b} coupling, may affect the width of our considered decay channel $H \rightarrow b\bar{b}$. However, it is found that $C_{b\phi}$ is severely constrained already from several studies [75, 76, 132, 133], and within its constrained range ($\sim \pm 10^{-3}$), the basic kinematic distributions of the tHq process do not receive any visible effect. Thus, we have not included the impact of $\mathcal{O}_{b\phi}$ on the $H \rightarrow b\bar{b}$ decays in our analysis. Moreover, the impact of other SMEFT operators to the H-V-V (V=W,Z) couplings, such as $\mathcal{O}_{\phi W/D}$ may have some effect to the total decay width of Higgs. However, due to the strong constraints on $\mathcal{O}_{\phi D}$, as argued earlier, we do not consider this operator in Higgs boson decays and move on with $\mathcal{O}_{\phi W}$ only. On the contrary, EFT effects on the top quark decay vertex (W-t-b) are taken into consideration as it is expected to provide a similar impact as in the production vertex. Thus the $\mathcal{O}_{\phi Q}^{(3)}$, and \mathcal{O}_{tW} play important roles through the W-t-b vertex in the tHq production and subsequent decay of the top-quark. The other operator, such as $\mathcal{O}_{t\phi}$ affects the tHq production through the t- \bar{t} -H

vertex, whereas $\mathcal{O}_{Qq}^{(3,1)}$ and $\mathcal{O}_{Qq}^{(3,8)}$ contribute via the 4-Fermion (4-F) interaction, including additional Feynman diagrams.

Finally, having all these considerations, we end up with the following six relevant set of operators for our present study,

$$\mathcal{O}_{t\phi}, \mathcal{O}_{\phi Q}^{(3)}, \mathcal{O}_{tW}, \mathcal{O}_{Qq}^{(3,1)}, \mathcal{O}_{Qq}^{(3,8)}, \mathcal{O}_{\phi W}. \quad (2.2)$$

Now onward, in the text, SMEFT operators will refer to this set of six operators only. It is to be noted that several studies based on global fits have already restricted the WCs of these operators, considering a set of large number of experimental measurements [75, 76]. In this present study, we revisit the constraints of the WCs corresponding to these set of SMEFT operators (Eq. 2.2) taking into account the latest experimental measurements, which are sensitive to these operators. In addition, some of the new measurements from CMS and ATLAS experiments, that were not taken into consideration in the previous studies [106, 112, 127–131, 134, 135], are included in our analysis. In the next section, we systematically describe our methodology of constraining these operators.

3 Constraining operators $\mathcal{O}_{t\phi}, \mathcal{O}_{\phi Q}^{(3)}, \mathcal{O}_{tW}, \mathcal{O}_{Qq}^{(3,1)}, \mathcal{O}_{Qq}^{(3,8)}, \mathcal{O}_{\phi W}$

Setting the goal to constrain the set of chosen SMEFT operators, first we set up the framework to calculate the theoretical cross-section and other related observables of several physics processes of our interest in terms of the WCs. Subsequently, in order to understand the sensitivity of the SMEFT operators of our interest to any given physics process, we construct the Fisher Information Matrix (FIM) [136]. Finally, performing a χ^2 -fitting of the calculated expressions of the observables with the corresponding experimental measurements, best-fit values of the WCs along with the constrained ranges are presented.

3.1 Cross-section calculation

Inclusion of SMEFT operators to the SM lagrangian (Eq. 1.1) eventually leads to the modification of cross-sections and various related observables. Restricting terms only up to dimension-6 operators in the EFT expansion, the scattering amplitude of any physical process is given by,

$$\mathcal{M}_{tot} = \mathcal{M}_{SM} + \mathcal{M}_{EFT}(C_i), \quad (3.1)$$

and hence, the matrix element can be written as,

$$|\mathcal{M}_{tot}(C_i)|^2 = |\mathcal{M}_{SM}|^2 + 2Re[\mathcal{M}_{SM}^* \mathcal{M}_{EFT}(C_i)] + |\mathcal{M}_{EFT}(C_i)|^2. \quad (3.2)$$

Here $|\mathcal{M}_{SM}|^2$ resembles the SM part, while the second term corresponds to the interference between EFT and SM ($\propto 1/\Lambda^2$), which is generally responsible for the dominant EFT contribution. The third term being the quadratic one, is suppressed by $\propto 1/\Lambda^4$. The C_i

represents the WC for the i th operator, \mathcal{O}_i . Finally, the cross-section can be expressed in a more compact form as,

$$\sigma^{EFT}(C) = \sigma^{SM} + \sum_{i=1}^n C_i \beta_i + \sum_{j \leq k}^n C_j C_k \gamma_{jk}. \quad (3.3)$$

Here σ^{SM} is the standard model cross-section, ‘ n ’ is the total number of relevant SMEFT operators taken into account to the given process, while β, γ are process-dependent coefficients for the linear and quadratic terms respectively, setting $\Lambda = 1$ TeV. From now onwards, all numerical calculations in this study will assume $\Lambda = 1$ TeV. In general, in the case of differential cross-section calculation, these coefficients depend on the momenta and masses of particles involved in the process. While integrating out over momenta to obtain the total cross-section, these remain mass dependent only. Needless to say, the SM cross-section can be recovered by setting all the C_i to zero.

For some specific cases, the experimental measurements are also presented in terms of signal strengths, differential cross-section, asymmetry, etc., in addition to the total production cross-sections. Interestingly, all of these observables can be expressed, in a similar manner, in terms of a polynomial as Eq. 3.3. For instance, the signal strength for a given process, say, $pp \rightarrow tHq$ with $t/H \rightarrow xx$, where xx symbolizes the decay products, one can write,

$$\mu_{xx}^{EFT}(C) = \frac{\sigma_{xx}^{EFT}}{\sigma_{xx}^{SM}} = 1 + \sum_{i=1}^n a_i C_i + \sum_{j \leq k}^n b_{jk} C_j C_k. \quad (3.4)$$

Here, the coefficients a_i and b_{jk} are the function of momenta and masses of particles involved in the process and specific to particular decay channel $t/H \rightarrow xx$. The symbol “ xx ” being removed from the polynomial expression for simplicity (see Appendix A). The Eq. 3.4 is the most general expression for μ_{xx}^{EFT} up to the quadratic order in WCs for the full process including the decay chain (see Appendix A). Following the similar procedure, any observable related to the cross-section can be expressed as a polynomial in WCs having some process-dependent coefficients, such as, β_i, γ_{jk} or a_i, b_{jk} and so on.

In principle, the lagrangian including the SMEFT terms (Eq. 1.1) provides a framework which is calculable and predictive to find the impact of those operators to any process. However, it is quite complicated and also very exhaustive to obtain the analytical expressions of these coefficients, such as β_i, γ_{ij} or a_i, b_{ij} etc. for any chosen process. Instead, we follow a different approach. The numerical values of these coefficients are obtained by fitting of the cross-sections considering WCs as variables while β_i, γ_{ij} as fitting parameters. In this approach, first the variation of cross-section with the WCs is obtained, which is then fitted with an appropriate polynomial to find the numerical values of the corresponding coefficients. This strategy is described in detail below.

The cross-sections are calculated at the leading order (LO) approximation using `MG5aMC_atNLO` [137] interfacing with `SMEFTatNLO` [126] feynrules UFO. While doing the calculations,

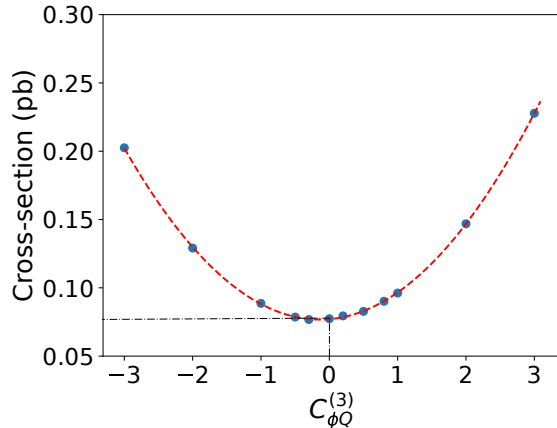


Figure 2: The cross-section of tH production process for different values of $C_{\phi Q}^{(3)}$ (solid points). The cross-section is fitted (dashed line) with a quadratic polynomial (Eq. 3.6).

we employ five-flavour scheme (5 FS) with NNPDF23L0 [138] for parton distribution function and set the dynamic QCD scale ($Q^2 = \frac{1}{2} \sum_{i=1}^{N_f} (m_i^2 + p_{Ti}^2)$; N_f = number of final state particles). A basic set of event generation kinematic selection cuts are applied wherever required, to obtain cross-sections only in the relevant fiducial region of phase space of any given process. The decays, wherever necessary, were performed using `Madspin`, allowing us to take into account the spin of mother particle into decay products.

Before presenting the full calculation, first we demonstrate our strategy by giving an example of calculating the cross-section of a process including a single WC (say C_1), and setting others to zero. With this assumption, any production cross-section (Eq. 3.3), with $t/H \rightarrow xx$, can be written as,

$$\sigma_{xx}^{\text{EFT}}(C_1) = \sigma^{\text{SM}} + \beta_1 C_1 + \gamma_{11} C_1^2. \quad (3.5)$$

For example, the variation of $\sigma_{xx}^{\text{EFT}}(C_1)$ for the tH (tHq+tHW) production for a range of values of $C_1 \equiv C_{\phi Q}^{(3)}$ produces a curve, quadratic in nature (Eq. 3.5), as shown in Fig. 2 by solid points.

Notice that the variation of the cross-section with WCs is almost symmetric around $C_{\phi Q}^{(3)} = 0$, i.e, does not depend on the sign of WC. It implies that the coefficient (β_1) of the linear term in Eq. 3.5 is insignificant in comparison to that of the quadratic term (γ_{11}). Now we perform a polynomial fitting of these points representing the cross-section. The fitted curve is shown as a dashed line in Fig 2, and the corresponding polynomial expression is given by,

$$\sigma_{xx}^{\text{EFT}}(C_{\phi Q}^{(3)})[\text{pb}] = 0.077 + 0.004 C_{\phi Q}^{(3)} + 0.015 C_{\phi Q}^{(3)2}. \quad (3.6)$$

It confirms our observation that the interference term (with coefficient $\beta_1 = 0.004$) contributes to negligible level in this case. Needless to say that the cross-section for $C_{\phi Q}^{(3)} =$

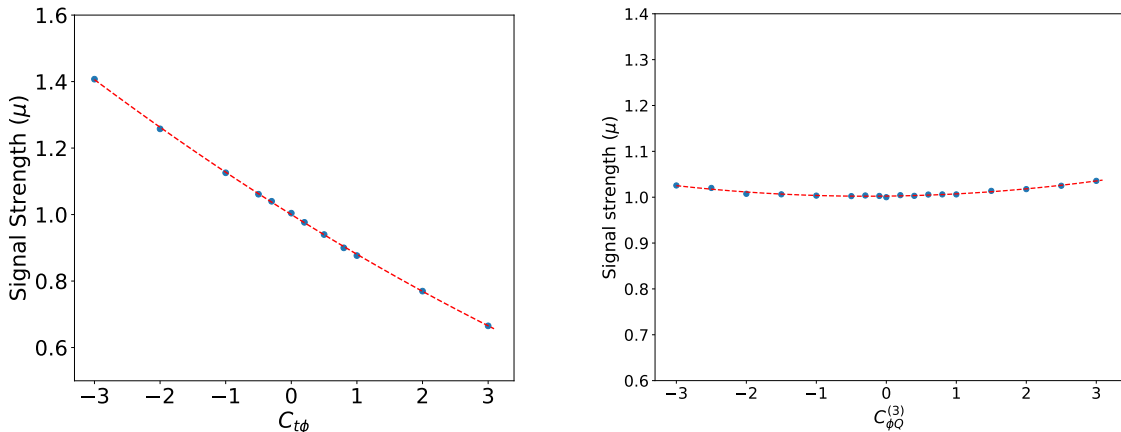


Figure 3: The signal strength for $t\bar{t}H$ production for different values of $C_{t\phi}$ (left) and $C_{\phi Q}^{(3)}$ (right), fitted (dashed line) with a quadratic polynomial.

$C_1 = 0$ represents for SM tH production cross-section, $\sigma^{SM} = 0.077$ pb, and it is found to be consistent with the existing calculation in the literature [139].

For another illustration, we repeat this exercise by studying the variation of $t\bar{t}H$ signal strength (μ) with the operator $C_{t\phi}$ or $C_{\phi Q}^{(3)}$ setting all the other WCs to zero. Fig. 3 presents the variation of μ with $C_{t\phi}$ (left) and $C_{\phi Q}^{(3)}$ (right). The negative slope of the μ with $C_{t\phi}$ indicates that the interference term, linear in WC, is the dominant one compared to the quadratic term. The almost constant behavior of the cross-section with $C_{\phi Q}^{(3)}$ implies that the $t\bar{t}H$ process is not much sensitive to this operator. In these cases, a linear approximation is good enough to fit the μ .

In case of two non-zero SMEFT operators, i.e $n = 2$, the same procedure is followed by setting two operators of interest to non-zero values, keeping all others to zero. Accordingly, the production cross-sections for a given process can be expressed in terms of two WCs following Eq. 3.3,

$$\sigma_{xx}^{EFT}(C_1, C_2) = \sigma^{SM} + \beta_1 C_1 + \beta_2 C_2 + \gamma_{11} C_1^2 + \gamma_{22} C_2^2 + 2\gamma_{12} C_1 C_2. \quad (3.7)$$

Note that, the quadratic terms are suppressed by Λ^4 , and hence are not considered in several analysis [50, 52, 75]. Following the same strategy as before, the numerical values of these coefficients can be obtained by fitting their variation of cross-sections with the corresponding combination of WCs. The procedure is same for other observables, such as, signal strength (μ), asymmetry, etc. Here, the variation of the $t\bar{t}H$ signal strength with WCs $C_{\phi Q}^{(3)}$ and $C_{t\phi}$ is fitted with a two dimensional quadratic polynomial. The expression of the fitted polynomial the $t\bar{t}H$ signal strength is found to be of the form,

$$\begin{aligned} \mu^{EFT}(C_{\phi Q}^{(3)}, C_{t\phi}) = & 1.0 + 0.002 C_{\phi Q}^{(3)} + 0.002 C_{\phi Q}^{(3)2} - 0.122 C_{t\phi} \\ & + 0.004 C_{t\phi}^2 - 0.001 C_{\phi Q}^{(3)} C_{t\phi}, \end{aligned} \quad (3.8)$$

where the leading term corresponds to the SM signal strength. The above expression indicates that the operator corresponding to the WC $C_{t\phi}$ has comparatively more dominant effect on the $t\bar{t}H$ process. An important point to note here is that, for any given physical process and center of mass energy, the numerical values of the coefficients of a given term are unique and independent, i.e, not correlated with the values of other WCs. Repeating the similar exercise, the numerical coefficients for all the 5 operators (Eq. 2.2) for the $t\bar{t}H$ signal strength are obtained. For the sake of illustration, the numerical values of the coefficients for the linear (C_i), quadratic (C_i^2) and interference terms ($C_i C_j$) for the tH production cross-section and the $t\bar{t}H$ signal strength are presented in Table 2(a) and Table 2(b), respectively. Here the (1,1) entries present the expected SM cross-section for the tH production, whereas other values in the first row represent the values of coefficients for the linear terms. The diagonal entries present the numerical values corresponding to the quadratic terms, while others show the same for the interference terms. We present the Monte-Carlo uncertainties for each of the entries in these tables. For several entries, the uncertainties are much smaller than the values of the coefficients (β_i, γ_{jk} , or a_i, b_{jk} , see Eq. 3.3, 3.4). The operators corresponding to these entries have a non-zero effect on the considered process. On the other hand, for a few entries, e.g., the interference terms between $C_{Qq}^{(3,8)}$ and other operators in Table 2(a), the uncertainties are found to be larger than the values of the coefficients (γ_{jk}). These can be interpreted as the irrelevance of the corresponding terms to the process, and the non-zero values of the entries arise solely due to uncertainties in the calculation. These tables explicitly show how an individual operator, or two operators in combination, affect a given process. For instance, in the case of $C_{t\phi}$ in Table 2(b), the value of the coefficient for the linear term with a negative sign and smaller value for the same for quadratic term justify the pattern of variation of signal strength shown in Fig. 3 (left). Similarly, the tiny values of coefficients of $C_{\phi Q}^{(3)}$ justify the curve in the same figure (right). Table 2(b) also suggests that $C_{Qq}^{(3,1)}, C_{Qq}^{(3,8)}$ and $C_{t\phi}$ are comparatively more sensitive to the $t\bar{t}H$ process. On the other hand, Table 2(a) indicates that $C_{tW}, C_{Qq}^{(3,1)}$, and $C_{\phi Q}^{(3)}$ have the dominant sensitivity to the tH production process. Following this exercise, eventually, we obtain the WC-dependent functional forms of the cross-section and other observables such as signal strength, differential cross-section, asymmetry etc. for each of the processes considered in this study, precisely what we need in the next step to interpret precision measurements.

3.2 Experimental measurements

In this subsection, we present the list of measurements used as inputs in our analysis, to constrain the SMEFT operators.

- **Production of Higgs boson:** Several Higgs-boson production modes are relevant to the considered set of operators in Eq. 2.2. For example, the production of Higgs boson in association with vector bosons (WH and ZH) and the vector boson fusion (VBF) include

Table 2: The coefficients of various linear (β_i, a_i) and quadratic terms (γ_{jk}, b_{jk}), following Eq 3.3 and 3.4, corresponding to the fits for the cross-section of tH and the signal strength (μ) of $t\bar{t}H$.

(a) Coefficients (β_i, γ_{jk}) for the fits of tH cross-section (units in pb)

	1	$C_{t\phi}$	$C_{\phi Q}^{(3)}$	C_{tW}	$C_{Qq}^{(3,1)}$	$C_{Qq}^{(3,8)}$	$C_{\phi W}$
1	$7.7E-2 \pm 5.0E-5$	$-3.4E-3 \pm 2.4E-5$	$3.9E-3 \pm 4.0E-5$	$2.2E-2 \pm 8.0E-5$	$-9.7E-3 \pm 1.4E-4$	$1.9E-4 \pm 8.0E-5$	$1.1E-3 \pm 2.6E-5$
$C_{t\phi}$		$9.1E-3 \pm 1.2E-5$	$-4.0E-3 \pm 2.5E-5$	$-1.9E-3 \pm 5E-5$	$4.6E-3 \pm 7.0E-5$	$-1.0E-5 \pm 4.0E-5$	$-8.8E-4 \pm 1.5E-5$
$C_{\phi Q}^{(3)}$			$1.5E-2 \pm 2.0E-5$	$5.0E-3 \pm 7.0E-5$	$-1.4E-2 \pm 1.0E-4$	$2.0E-5 \pm 5.0E-5$	$4.0E-3 \pm 1.7E-5$
C_{tW}				$6.5E-2 \pm 5.0E-5$	$5.9E-3 \pm 1.6E-4$	$4.0E-4 \pm 9.0E-5$	$1.1E-2 \pm 1.7E-5$
$C_{Qq}^{(3,1)}$					$1.6E-1 \pm 1.1E-4$	$1.0E-5 \pm 1.3E-4$	$-5.0E-3 \pm 7.0E-5$
$C_{Qq}^{(3,8)}$						$3.5E-2 \pm 8.0E-5$	$1.2E-5 \pm 3.0E-5$
$C_{\phi W}$							$6.3E-3 \pm 3.2E-5$

(b) Coefficients (a_i, b_{jk}) for the fits of $t\bar{t}H$ signal strength (μ)

	1	$C_{t\phi}$	$C_{\phi Q}^{(3)}$	C_{tW}	$C_{Qq}^{(3,1)}$	$C_{Qq}^{(3,8)}$	$C_{\phi W}$
1	$1.00 \pm 1.1E-4$	$-1.23E-1 \pm 1.7E-4$	$2.0E-3 \pm 1.7E-4$	$9.2E-3 \pm 1.9E-4$	$1.9E-2 \pm 2.9E-4$	$1.6E-2 \pm 2.1E-4$	$1.1E-3 \pm 1.9E-4$
$C_{t\phi}$		$3.8E-3 \pm 8.0E-5$	$-8.8E-4 \pm 1.0E-4$	$-3.4E-4 \pm 1.1E-4$	$-1.1E-3 \pm 1.5E-4$	$-7.6E-4 \pm 1.1E-4$	$-1.1E-4 \pm 9.0E-5$
$C_{\phi Q}^{(3)}$			$2.6E-3 \pm 7E-5$	$-8.6E-3 \pm 1.2E-4$	$2.8E-4 \pm 1.7E-4$	$1.0E-5 \pm 1.2E-4$	$1.4E-4 \pm 1.1E-4$
C_{tW}				$2.6E-2 \pm 9.0E-5$	$5.3E-2 \pm 1.9E-4$	$3.0E-5 \pm 1.4E-4$	$2.1E-3 \pm 1.2E-4$
$C_{Qq}^{(3,1)}$					$1.26E-1 \pm 1.4E-4$	$9.0E-5 \pm 1.9E-4$	$7.2E-3 \pm 1.7E-4$
$C_{Qq}^{(3,8)}$						$2.8E-2 \pm 1.1E-4$	$6.0E-5 \pm 1.2E-4$
$C_{\phi W}$							$1.5E-4 \pm 9.0E-5$

the V-V-H vertex in the production diagram. They are thus crucial to the SMEFT operator $\mathcal{O}_{\phi W}$. On the other hand, top-quark production, either in pair or in single, in association with the SM Higgs boson, namely $t\bar{t}H$, tHq , and tHW processes, as shown in Table 3, are sensitive to the rest of the operators in Eq. 2.2. The measurements are presented in terms of signal strength (μ) as defined in Eq 3.4, including uncertainties and for various luminosity options. In case of asymmetric error, the larger value is taken into consideration.

- **Single top-quark production:** This set of data includes only the single top-quark production along with a jet in the t-channel process. However, the single top quark production in association with a W boson (tW production) is treated in a different category. These measurements are mostly sensitive to $C_{\phi Q}^{(3)}$ and C_{tW} via the W-t-b vertex, as seen in Table 8. The measurements include mainly the total production cross-sections and as well as normalized differential cross-sections, listed in Table 4. The added advantage of using normalized differential cross-sections is to have the minimal effect of uncertainties in comparing the theoretical predictions (LO) to the observed one. Although there are several differential cross-section measurements corresponding to different observables, in this study, we have considered only one ($\frac{1}{\sigma} \frac{d\sigma}{d|y|}$) of them, since others must be highly correlated.

- **Top-quark pair production and $t\bar{t}$ asymmetry:** There are a good number of

Table 3: Measurements of associated production of single-top and top-pair with Higgs boson, with μ being the signal strength.

	Process	Observable	\mathcal{L} (fb $^{-1}$)	Measured value	Ref.
ATLAS	VBF, H \rightarrow WW	μ	139	$0.93^{+0.23}_{-0.20}$	[140]
	VBF, H \rightarrow $\tau\tau$	μ	139	$0.90^{+0.20}_{-0.17}$	[114]
	VBF, H \rightarrow $b\bar{b}$	μ	126	$0.95^{+0.33}_{-0.32}$	[141]
	ZH, H \rightarrow WW	μ	139	$1.64^{+0.55}_{-0.47}$	[142]
	WH, H \rightarrow WW	μ	139	$0.45^{+0.32}_{-0.29}$	[142]
	$t\bar{t}$ H, H \rightarrow $b\bar{b}$	μ	79.8	$0.79^{+0.61}_{-0.60}$	[112]
	$t\bar{t}$ H, H \rightarrow ZZ(4ℓ)	μ	79.8	< 1.77 at 68% CL	[112]
	$t\bar{t}$ H, H \rightarrow Multi-lepton	μ	79.8	$1.56^{+0.42}_{-0.40}$	[112]
CMS	VBF, H \rightarrow WW	μ	138	$0.71^{+0.28}_{-0.25}$	[143]
	VBF, H \rightarrow $\gamma\gamma$	μ	137	$1.04^{+0.34}_{-0.31}$	[144]
	ZH, H \rightarrow WW	μ	138	$2.0^{+0.7}_{-0.7}$	[143]
	ZH, H \rightarrow $\tau\tau$	μ	138	$2.0^{+0.91}_{-0.81}$ (bin 1) $2.18^{+1.0}_{-0.82}$ (bin 2)	[145]
	WH, H \rightarrow WW	μ	138	$2.0^{+0.6}_{-0.6}$	[143]
	WH, H \rightarrow $\tau\tau$	μ	138	$0.79^{+0.94}_{-0.91}$ (bin 1) $2.65^{+1.26}_{-1.15}$ (bin 2)	[145]
	$t\bar{t}$ H, H \rightarrow $b\bar{b}$	μ	138	$-0.27^{+0.86}_{-0.83}$	[135]
	$t\bar{t}$ H, H \rightarrow $b\bar{b}$	μ	35.9	$0.72^{+0.45}_{-0.45}$	[106]
	$t\bar{t}$ H, H \rightarrow ZZ(4ℓ)	μ	137	$0.16^{+0.98}_{-0.16}$	[128]
	$t\bar{t}$ H, H \rightarrow Multi-lepton	μ	35.9	$1.23^{+0.45}_{-0.43}$	[134]
	tHq + tHW, combined	σ	35.9	$0.92^{+0.40}_{-0.27}$ pb	[127]

measurements of the top-quark pair production and the $t\bar{t}$ asymmetry, but here we focus only on some most sensitive recent measurements (see Table 5). We particularly used the differential cross-section measurements for $t\bar{t}$. Though differential distributions in various kinematic bins are measured, we considered one of them from each analysis to avoid unknown experimental correlations between pairs of distributions, which might lead to double counting.

These measurements are mostly sensitive to the four-fermi operators ($C_{Qq}^{(3,1)}$ and $C_{Qq}^{(3,8)}$) (see Table 8).

• **Top-quark pair production in association with a vector boson:** In this category of measurements, $t\bar{t}Z$ and $t\bar{t}W$ processes are considered. It includes the measurements of total inclusive cross-sections and differential cross-section like single top case, as shown in Table 6. This set of data is primarily useful in constraining $C_{\phi Q}^{(-)}$ and $C_{\phi t}$ (see table 8). For both the processes, the combined measurements with the final states consisting of 3ℓ

Table 4: Measurements of single top-quark production and normalized differential cross-sections, in terms of the rapidity (y) of the reconstructed top-quark.

	Process	Observable	\mathcal{L} (fb $^{-1}$)	Measured value	Ref.
CMS	tj (t-channel)	$\sigma_{\text{tot}}(t)$	35.9	130 ± 19 pb	[146]
	tj (t-channel)	$\sigma_{\text{tot}}(\bar{t})$	35.9	77 ± 12 pb	[146]
	tj (t-channel)	$(1/\sigma)d\sigma/d y^{t+\bar{t}} $	2.3	0.64 ± 0.14 (bin 1)	[147]
				0.55 ± 0.12 (bin 2)	
				0.50 ± 0.12 (bin 3)	
				0.18 ± 0.08 (bin 4)	
		$(1/\sigma)d\sigma/d y^t $	35.9	0.58 ± 0.15 (bin 5)	[148]
				0.53 ± 0.08 (bin 6)	
				0.50 ± 0.09 (bin 7)	
			0.47 ± 0.09 (bin 8)		
			0.26 ± 0.02 (bin 9)		
ATLAS	tj (t-channel)	$\sigma_{\text{tot}}(t)$	3.2	156 ± 28 pb	[149]
	tj (t-channel)	$\sigma_{\text{tot}}(\bar{t})$	3.2	91 ± 19 pb	[149]

Table 5: Measurements of $t\bar{t}$ charge-asymmetry (A_C) and normalized top-quark pair production differential cross-sections, in terms of the invariant mass ($m_{t\bar{t}}$) of the top pair.

	Process	Observable	\mathcal{L} (fb $^{-1}$)	Measured value	Ref.
ATLAS	$t\bar{t}$	$(1/\sigma)d\sigma/dm_{t\bar{t}}$	139	0.21 ± 0.0023 (bin 3)	[85]
				0.25 ± 0.003 (bin 4)	
				0.18 ± 0.0035 (bin 5)	
				0.11 ± 0.0044 (bin 6)	
CMS	$t\bar{t}$	$(1/\sigma)d\sigma/dm_{t\bar{t}}$	137	0.10 ± 0.15 (bin 1)	[150]
				0.16 ± 0.08 (bin 2)	
				0.21 ± 0.09 (bin 3)	
				0.20 ± 0.09 (bin 4)	
				0.14 ± 0.02 (bin 5)	
				0.08 ± 0.02 (bin 6)	
				0.05 ± 0.02 (bin 7)	
				0.28 ± 0.02 (bin 8)	
ATLAS	$t\bar{t}$	A_C	139	0.0060 ± 0.0015	[151]
CMS	$t\bar{t}$	A_C	138	$0.69^{+0.65}_{-0.69}$	[152]

and 4ℓ are considered and the corresponding theoretical cross sections are also estimated according to those final states.

Table 6: Measurements of associated production of top-quark pair with a vector boson.

	Process	Observable	\mathcal{L} (fb $^{-1}$)	Measured value	Ref.
ATLAS	$t\bar{t}Z$	σ_{tot}	36.1	0.95 ± 0.13 pb	[79]
	$t\bar{t}W$	σ_{tot}	36.1	0.87 ± 0.19 pb	[79]
	$t\bar{t}Z$	$(1/\sigma)d\sigma/dp_T^Z$	139	0.0018 ± 0.0013 (bin 1)	[131]
				0.0055 ± 0.0025 (bin 2)	
				0.0053 ± 0.002 (bin 3)	
				0.0057 ± 0.0015 (bin 4)	
				0.0022 ± 0.00085 (bin 5)	
CMS	$t\bar{t}Z$	μ	138	$0.65^{+1.04}_{-0.98}$	[135]
	$t\bar{t}Z$	σ_{tot}	35.9	0.99 ± 0.14 pb	[153]
	$t\bar{t}W$	σ_{tot}	35.9	0.77 ± 0.17 pb	[153]
	$t\bar{t}Z$	σ_{tot}	77.5	0.95 ± 0.08 pb	[93]
	$t\bar{t}Z$	$(1/\sigma)d\sigma/dp_T^Z$	77.5	0.004 ± 0.001 (bin 1)	[93]
				0.005 ± 0.0009 (bin 2)	
				0.0022 ± 0.0005 (bin 3)	
			0.0003 ± 0.0001 (bin 4)		

• **Single top-quark production in association with vector boson:** This category includes tZq and tW production both in ATLAS and CMS experiments and the measurements of the total and differential cross-sections are taken into account. The lists of measurements used in the analysis are shown in Table 7. According to Table 8, these measurements mainly restrict $C_{\phi Q}^{(3)}$.

3.3 Fisher information matrix

In order to have a quantitative assessment of the level sensitivity of these SMEFT operators to various processes, we resort to the formalism of the FIM [136]. The FIM provides a quantitative comparison of sensitivity of a given set of SMEFT operators among a set of processes.

Defining $f(X|\vec{C})$ as the distribution of the experimental measurements X and the given true values of the set of WCs \vec{C} , the FIM is defined as [136]

$$I_{ij}(\vec{C}) = -E \left[\frac{\partial^2 \log f(X|\vec{C})}{\partial C_i \partial C_j} \right], \quad (3.9)$$

where ‘E’ represents the expectation value over a set of measurements X , and indices i, j stand for the labels of WCs. One can argue that the smallest uncertainty for the WC (C_i)

Table 7: Measurements of associated production of single top-quark with vector boson.

	Process	Observable	\mathcal{L} (fb $^{-1}$)	Measured value	Ref.
CMS	tZq(1 $^+$, 2 ℓ)	σ_{tot}	138	62.2 $^{+7.4}_{-6.8}$ fb	[129]
	tZq(1 $^-$, 2 ℓ)	σ_{tot}	138	26.1 $^{+5.6}_{-5.4}$ fb	[129]
	tW	σ_{tot}	36	89 \pm 13 pb	[130]
	tW	σ_{tot}	35.9	63 \pm 7 pb	[154]
	tZ	1/ $\sigma d\sigma/dp_T^Z$	138	0.007 \pm 0.002(bin 1) 0.002 \pm 0.007(bin 2) 0.0026 \pm 0.001(bin 3) 0.0008 \pm 0.0004(bin 4)	[129]
ATLAS	tZ	σ_{tot}	139	97 \pm 15 pb	[155]
	tW	σ_{tot}	3.2	94 $^{+30}_{-24}$ pb	[156]

can be obtained using the Cramer-Rao bound on the covariance matrix $\text{Cov}_{ij}(\vec{C})$ [157],

$$\text{Cov}_{ij} \geq (I^{-1})_{ij}. \quad (3.10)$$

If there are N_{exp} number of measurements of an observable ‘X’, which depend on the N_{WC} number of WCs, then assuming $f(X|\vec{C})$ to be Gaussian like as,

$$f(X|\vec{C}) = \prod_{m=1}^{N_{\text{exp}}} \frac{1}{\sqrt{2\pi\delta_{\text{exp},m}^2}} \exp \left[-\frac{\left(X_m^{\text{exp}} - X_m^{\text{EFT}}(\vec{C})\right)^2}{2\delta_{\text{exp},m}^2} \right], \quad (3.11)$$

the expanded form of FIM can be constructed following Eq. 3.9 [76],

$$I_{ij} = E \left[\sum_{m=1}^{N_{\text{exp}}} \frac{1}{\delta_{\text{exp},m}^2} \left(\gamma_{m,ij} (X_m^{\text{EFT}} - X_m^{\text{exp}}) + \left(\beta_{m,i} + \sum_{l=1}^{N_{\text{WC}}} C_l \gamma_{m,il} \right) \left(\beta_{m,j} + \sum_{l'=1}^{N_{\text{WC}}} C_{l'} \gamma_{m,jl'} \right) \right) \right] \quad (3.12)$$

Here δ_{exp} is the experimental uncertainty, β and γ are the numerical values of the linear and quadratic coefficients of the theoretical expression of observable X respectively (see, e.g., Eq. 3.3 when $X^{\text{EFT}} \equiv \sigma^{\text{EFT}}$). Now, following the procedure described in Ref. [136], we define a six-dimensional basis of WCs as,

$$\vec{C} \equiv \left(C_{\phi Q}^{(3)} \quad C_{Qq}^{(3,8)} \quad C_{Qq}^{(3,1)} \quad C_{t\phi} \quad C_{tW} \quad C_{\phi W} \right)^T. \quad (3.13)$$

With this choice, I_{ij} is evaluated for a set of processes, such as tH, t \bar{t} H, single-top, t \bar{t} V (V = W, Z), tZq and tW. After diagonalization of I_{ij} , the diagonal entries quantify the level of sensitivity of the i^{th} WC (C_i) to a given physical process. In other words, those present the values of sensitivity of a given process to the i^{th} WC. This quantification indicates the relative strength by which the i^{th} WC can be constrained from the measurements of that process. For the sake of illustration, the FIM for the set of \vec{C} (Eq. 3.13) considering the single-top (tj) production and differential cross-section measurements (see Table 4) is given by,

$$\begin{bmatrix} 9.52 & 0.27 & -11.20 & 0 & 3.25 & 0 \\ 0.27 & 89.29 & 2.63 & 0 & 0.48 & 0 \\ -11.20 & 2.64 & 588.81 & 0 & 12.38 & 0 \\ 0 & 0 & 0 & 0 & 0 & 0 \\ 3.25 & 0.48 & 12.38 & 0 & 20.20 & 0 \\ 0 & 0 & 0 & 0 & 0 & 0 \end{bmatrix}.$$

The corresponding eigenvalues are $\text{diag}(I_{ij}) = \{8.30, 89.28, 589.27, 0, 20.96, 0\}$. The set of diagonal entries of diagonalized I_{ij} matrix clearly indicates that $C_{Qq}^{(3,1)}$ is most sensitive to single-top production, followed by $C_{Qq}^{(3,8)}$. The effect of other WCs, such as, $C_{\phi Q}^{(3)}$ and C_{tW} are almost negligible. Since, only the relative size of the entries of the I_{ij} is important, not the absolute size, we normalize these entries in such a way that $\sum_{i=1}^{N_{\text{WC}}} |\text{diag}(I_{ii})| = 100$. It gives a normalized measure of the relative sensitivity of the WCs for a given process. Following the above strategy, the FIM for all our considered processes and operators are derived and presented in Table 8(a). On the other hand, relative sensitivities of different processes to a given operator depend on the relative sizes of the same diagonal entries (say, (k, k) , where $k = 1, \dots, 6$, with (1,1) for $C_{\phi Q}^{(3)}$, (2,2) for $C_{Qq}^{(3,8)}$, and so on.) for the FIMs corresponding to respective processes. Thus, in this case, we normalize entries for individual operators over all processes, such as $\sum_{n=1}^{N_{\text{proc}}} |\text{diag}(I_{kk})|^{(n)} = 100$. Following this exercise, we present the sensitivities of an operator to different processes in Table 8(b).

Each column of the Table 8(a) presents the relative sensitivities of the set of WCs corresponding to respective physics processes. For instance, the operator corresponding to WCs $C_{Qq}^{(3,1)}$ and $C_{Qq}^{(3,8)}$ are primarily sensitive to all processes except tW production, where the 4-F vertex is not present. On the other hand, Table 8(b) helps understand the effects of different processes on individual operators. This table shows that the tH measurement is more effective in constraining the operators $\mathcal{O}_{\phi Q}^{(3)}$, \mathcal{O}_{tW} , and $\mathcal{O}_{t\phi}$ than other processes. However, it does not significantly impact the 4-Fermi and the $\mathcal{O}_{\phi W}$, where other Higgs boson or top-quark-related measurements are more effective. The information provided by this table are very useful in selecting the set of dataset to constrain a given set of SMEFT operators. This exercise leads us to conclude that the measurements related to the top quark production either in single or in pair, in association with Higgs and vector bosons are very useful to constrain the set of operators considered in this analysis.

3.4 Constraining WCs

In the earlier sections, we have laid out the theoretical setup and discussed in detail the level of sensitivity of each of the SMEFT operators (Eq. 3.9) with the processes involving top-quark (see Table 8). Accordingly, the list of precision measurements to be used as input is also identified. With all these settings, now we are set to find the constrained values of these six WCs by the method of χ^2 -minimization.

Table 8: The relative sensitivity of WCs to various processes after normalizing to the scale of 100, and computed using measurements from Table 3-7. Entries below 1% are dropped, except for the entries of the tH process. Also, $V \equiv W, Z$ wherever relevant.

(a) Normalization performed for individual processes.

WC	tH	t \bar{t} H	VBF	ZH	WH	tj	t \bar{t} V	tZ	tW	AC	t \bar{t}
$C_{\phi Q}^{(3)}$	14.5	-	-	-	-	1.2	-	1.1	52.5	-	-
$C_{Qq}^{(3,8)}$	2.2	13.0	-	-	-	12.5	11.8	11.7	-	77.1	32.3
$C_{Qq}^{(3,1)}$	11.1	81.1	-	-	-	83.2	88.1	81.0	-	22.5	67.1
$C_{t\phi}$	1.3	5.7	-	-	-	-	-	-	-	-	-
C_{tW}	70.6	-	-	-	-	2.9	-	5.6	47.3	-	-
$C_{\phi W}$	0.3	-	100	100	100	-	-	-	-	-	-

(b) Normalization performed for individual operators.

WC	tH	t \bar{t} H	VBF	ZH	WH	tj	t \bar{t} V	tZ	tW	AC	t \bar{t}
$C_{\phi Q}^{(3)}$	68.7	-	-	-	-	4.4	-	14.4	11.9	-	-
$C_{Qq}^{(3,8)}$	1.6	-	-	-	-	6.6	5.2	40.5	-	30.4	15.1
$C_{Qq}^{(3,1)}$	1.0	-	-	-	-	5.1	4.9	34.2	-	54.1	-
$C_{t\phi}$	74.1	24.8	-	-	-	-	-	-	-	-	-
C_{tW}	71.9	-	-	-	-	1.9	-	22.9	3.3	-	-
$C_{\phi W}$	0.5	-	31.8	26.9	40.7	-	-	-	-	-	-

For a given set of WCs, \vec{C} , the χ^2 function is defined as,

$$\chi^2(\vec{C}) = \frac{1}{N_{\text{dat}}} \sum_{i,j=1}^{N_{\text{dat}}} \left(\mathcal{O}_i^{\text{exp}} - \mathcal{O}_i^{\text{th}}(\vec{C}) \right) [\text{Cov}_{ij}]^{-1} \left(\mathcal{O}_j^{\text{exp}} - \mathcal{O}_j^{\text{th}}(\vec{C}) \right), \quad (3.14)$$

where, $\mathcal{O}_i^{\text{exp}}$ and $\mathcal{O}_i^{\text{th}}$ are the measured and theoretical values of the i -th observables, which can be total or differential cross-section, signal strength etc. Here N_{dat} represents the total number of data used in the χ^2 -minimization. The covariance matrix Cov_{ij}^{-1} contains the experimental and theoretical uncertainties. The χ^2 -minimization is performed using the framework of TMinuit with the option MIGRAD [158].

The convergence of MIGRAD method of χ^2 -minimization was confirmed, and the stability of the best-fit values are also checked with respect to different initial conditions of the WCs and the step sizes. The quality of χ^2 -minimization is ensured by verifying the quantity χ^2/N_{dat} , which turned out to be 0.9 (1.4) in case of linear (quadratic) fit for a total number of data, $N_{\text{dat}} = 70$.

We perform the fitting for two cases. In the first case, a given WC is fitted setting others to zero and label it as ‘‘single fit’’. Whereas, for the second case, fitting is carried out for all the operators, calling it a ‘‘combined fit’’. Depending on the order of the used

Table 9: Linear fit of WCs, for both the single and the combined fit, using the full dataset Table 3-7.

	$C_{t\phi}$	$C_{\phi Q}^{(3)}$	C_{tW}	$C_{Qq}^{(3,1)}$	$C_{Qq}^{(3,8)}$	$C_{\phi W}$
Single fit	$-1.0_{-1.7}^{+1.7}$	$2.0_{-1.3}^{+1.3}$	$0.8_{-2.2}^{+2.2}$	$-0.3_{-0.9}^{+0.9}$	$0.5_{-1.4}^{+1.5}$	$1.3_{-0.6}^{+0.6}$
Combined fit	$-1.9_{-3.4}^{+3.4}$	$2.2_{-2.3}^{+2.2}$	$2.0_{-3.0}^{+3.0}$	$-0.4_{-0.45}^{+0.45}$	$0.7_{-1.4}^{+1.5}$	$1.2_{-0.6}^{+0.6}$

Table 10: Same as Table 9, but for quadratic fit of WCs.

	$C_{t\phi}$	$C_{\phi Q}^{(3)}$	C_{tW}	$C_{Qq}^{(3,1)}$	$C_{Qq}^{(3,8)}$	$C_{\phi W}$
Single fit	$-1.6_{-2.9}^{+3.7}$	$2.0_{-1.2}^{+1.0}$	$1.2_{-1.1}^{+0.5}$	$-0.2_{-0.5}^{+0.5}$	$-0.5_{-0.3}^{+0.4}$	$1.1_{-1.1}^{+0.7}$
Combined fit	$-0.45_{-3.1}^{+3.8}$	$-0.2_{-1.8}^{+3.4}$	$-1.3_{-0.7}^{+2.6}$	$-0.5_{-0.2}^{+1.3}$	$-0.2_{-0.4}^{+0.5}$	$1.0_{-1.2}^{+0.7}$

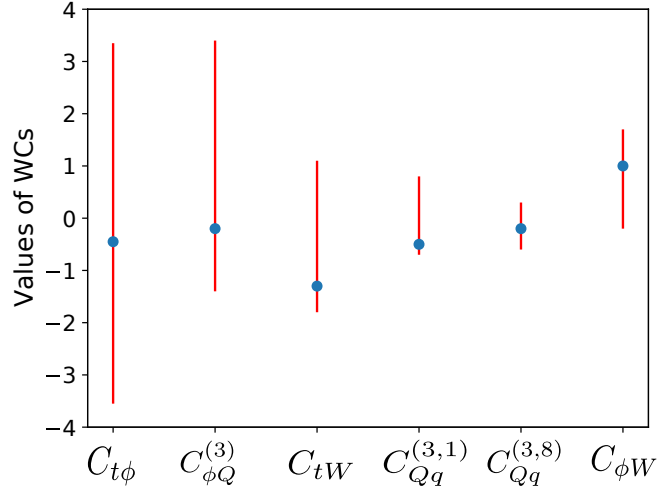


Figure 4: Best-fit values and corresponding allowed ranges for the WC, from combined quadratic fit (Table 10).

theoretical values, the fitting is performed both at linear and quadratic level (as shown in Eq 3.3). The results for both linear and quadratic fits are presented in Table 9 and Table 10 respectively, in terms of the best-fit values and the corresponding 2σ error. In each case, both the single fit and the combined fit scenarios are considered. For the sake of presentation, the best-fit values of the combined quadratic fit are also shown in Fig. 4, along with 2σ error bands.

Evidently, in the quadratic fitting, the magnitudes of the central values of the constrained WCs are reduced significantly, while the error bands remain almost unchanged. An exact matching between the theoretical prediction and the corresponding experimental measurements is expected to constrain WC severely, whereas, a wide gap between them may not be effective to put any tight constraint on them. In this regard, Table 8 predicts the set of datasets that can potentially constrain a subset of operators.

The systematics in the measured values translate the error in the fitted values of the WCs. For example, the C_{tW} operator affecting the vertex W - t - b is expected to be very sensitive to tH , tZ , and tW production, as seen in Table 8. Therefore, the measurements of cross-section, signal strength, or differential cross-section in various channels of these processes, as shown in Table 3, and 7, primarily constrain C_{tW} operator. Comparatively larger uncertainties in these measurements result in a substantial error to the best-fit value of C_{tW} . In contrast, 4-F operators are much more tightly constrained due to the measurements from tj , $t\bar{t}V$, $t\bar{t}A_C$, etc. Following similar arguments and considering Table 3-7, one can have some understanding of the best-fit values of the WCs as presented in Table 10. The uncertainties of theoretical cross-sections are not taken into consideration while performing fitting. However, we have checked that, a flat 10% theoretical uncertainty of all the observables affects the best-fit values of the WC with a shift by around 7 – 8%.

4 Implications at the LHC

The previous section presents the best-fit values within a constrained range of operators relevant to tHq process. The next goal is to explore the feasibility of finding the signal of these operators at the LHC with the present and future luminosity options. As mentioned before, the signal, if exists, is expected to be observed at the tail of the kinematic distribution of certain chosen observables constructed out of the momenta of final state particles of the tHq process. In this case, the primary reason for such possible deviations can be attributed to the energy growth in the scattering sub-amplitude $bW \rightarrow tH$ [122], where H is radiated off either from t or W boson.

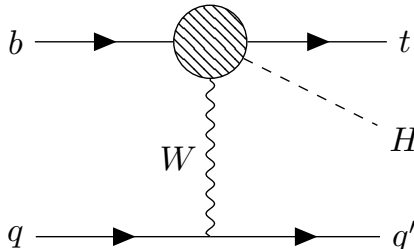


Figure 5: Representative Feynman diagram of tHq process, where the scattering sub-amplitude $bW \rightarrow tH$ can be embedded in the blob.

The presence of this sub-amplitude $bW \rightarrow tH$, in the tHq production process is shown in Fig. 5. Similar effects are also present in tZj , tWZ , and other production processes involving gauge or Higgs bosons, where different other scattering sub-amplitudes contribute to the energy growth [13, 159, 160]. On the contrary, these kinds of sub-amplitudes do not exist in the single-top, $t\bar{t}$, $t\bar{t}H$ or $t\bar{t}V$ processes, implying the absence of any energy growth due to the effect of the SMEFT operators. Consequently, while considering tHq process as the signal, even if these SMEFT operators may affect some of the dominating background

processes, especially the $t\bar{t}H$ production, the deviations in the kinematic distributions of the tHq process are expected to be visible over the background. Therefore, despite having a very low cross-section, the tHq production with a dedicated analysis strategy may turn out to be more promising compared to other common processes in probing the SMEFT effects at the LHC.

As already mentioned, the impact of the SMEFT operators on any process is very likely to be visible at the higher side of the kinematic distribution, supposed to be the signal region. With this understanding, we perform the analysis by splitting the phase space into two regions, (a) boosted region, with $p_T(H) > 300$ GeV, and (b) non-boosted region, with $p_T(H) < 300$ GeV. Additionally, both the hadronic and the leptonic decay channels of top-quark are considered separately. In the final state, the Higgs boson is reconstructed out of two b-jets, whereas the top quark is reconstructed as a top-jet for its hadronic decay mode only, for both the scenarios (a) and (b). In addition to the reconstructed top-quark and Higgs boson, the presence at least one non-tagged jet in the final state is required for both the cases. Additionally, a tagged b-jet is required for the leptonic final state. Thus, our signal final states are categorized as,

$$H_{\text{reco}} + t_{\text{reco}} + n\text{-jets} \quad (\text{hadronic final state}) \quad (4.1)$$

$$H_{\text{reco}} + \ell + n_b\text{-jets} + n\text{-jets} \quad (\text{semi-leptonic final state}), \quad (4.2)$$

with $n_b, n \geq 1$. The dominant SM background contributions are expected to be due to the following processes,

$$p p \rightarrow t\bar{t}, t\bar{t}H, t\bar{t}Z, t\bar{t}b\bar{b}, t\bar{t}W, WH. \quad (4.3)$$

Among these background processes, $t\bar{t}, t\bar{t}H, t\bar{t}Z, t\bar{t}b\bar{b}, t\bar{t}W$ contribute to both the hadronic and leptonic final state Eq. 4.1,4.2, while WH becomes important only for the leptonic final state Eq. 4.2.

In practice, the impact of SMEFT operators on any SM process are studied considering only one operator at a time setting others to zero, and then repeat this exercise for rest of the operators. In fact, initially we followed this strategy to understand the effects of individual operators to tHq process, which can be confirmed also by looking at the FIM (Eq. 3.9). However, in order to be realistic, effects of multiple relevant WCs are studied together to observe the combined effect, in particular due to the interference between different EFT operators and as well as with the SM. In our case, we set the values of the WCs to their respective best-fit as presented in Table 11 (copied from second row of the Table 10), which we dub as ‘‘SM+EFT’’, representing combined effects of the SM and the ‘EFT’ operators (Eq 1.1).

Table 11: Bestfit values of the WCs, referred together as ‘SM+EFT’.

	$\mathcal{O}_{t\phi}$	$\mathcal{O}_{\phi Q}^{(3)}$	\mathcal{O}_{tW}	$\mathcal{O}_{Qq}^{(3,1)}$	$\mathcal{O}_{Qq}^{(3,8)}$	$\mathcal{O}_{\phi W}$
Best-fit values	$-0.45^{+3.8}_{-3.1}$	$-0.2^{+3.4}_{-1.8}$	$-1.3^{+2.6}_{-0.7}$	$-0.5^{+1.3}_{-0.2}$	$-0.2^{+0.5}_{-0.4}$	$1.0^{+0.7}_{-1.2}$

4.1 Simulation of events and object selections

As before, the events are generated in MG5aMC_atNLO-3.3.0[137] using SMEFTatNLO UFO [126] package, which takes care of the SMEFT WCs. For decays, we use Madspin taking into account of the SMEFT effects, which is crucial for the top-quark decay. The showering and hadronization are performed using PYTHIA8[161, 162] followed by detector simulation using Delphes [163] with the choice of CMS specific detector card. The selection of the two different kinematic regions (a) and (b) are ensured by restricting Higgs boson p_T at the level of matrix element generation in Madgraph. The hard-scattered jets are required to have $p_T > 20$ GeV, while choosing MLM matching with XQCut 20 [164].

Apart from the signal events, this procedure is also followed for backgrounds with EFT effects, whereas, for SM-only backgrounds (i.e. all $C_i = 0$), the common SM UFO model in Madgraph5-aMC@NLO is used, instead of the SMEFTatNLO one. In case of WH production, leptonic mode of W decay is considered, since this background contributes only to the leptonic final state. Similar to the signal events, background events are also generated in p_T bins, namely, $300 < p_T < 600$ GeV (Bin 1) and $p_T > 600$ GeV (Bin 2), of bosons (H, Z or W) in $t\bar{t}h$, $t\bar{t}Z$, $t\bar{t}W$ events. For the generation of $t\bar{t}$ and $t\bar{t}b\bar{b}$ events, same selections are imposed on the p_T of the top-quark.

All the objects are reconstructed using Delphes inputs. In the following, the reconstruction procedure for different objects are described separately for two different regions (a) and (b), whereas the lepton selection is same for both the regions. The simulation strategy including the reconstructions of objects are described below.

(a) Boosted-region: To generate statistically appropriate number of events, the boosted category is further divided in two separate Higgs p_T bins, $300 < p_T(\text{H}) < 600$ GeV (Bin 1) and $p_T(\text{H}) > 600$ GeV (Bin 2).

Higgs-jet(HJ): First, e-flow objects of Delphes are used to construct fat-jets using Fastjet3.3.2[165] with Cambridge-Aachen[166] algorithm setting jet size parameter $R = 1.0$. Minimum p_T of the fatjets is set to be 300 GeV and 600 GeV for Bin-1 and Bin-2 respectively. These fat jets are then passed through mass-drop Tagger (MDT)[167, 168] setting $\mu = 0.667$ and $y_{\text{cut}} > 0.09$ to remove contamination due to soft radiation. The subjects of the ‘tagged fat jet’ are further matched with the b-quarks of the event which are selected within $|\eta| < 2.5$ and with a matching cone $\Delta R < 0.3$. When both the subjects are found to be b-like, and mass of the fat-jet lies within the window $m_J \in [100, 150]$, we identify the tagged fatjet as the HJ. The presence of B-hadron in the b-like subjects are found to exist for about 95% of the cases.

Top-jet(TopJ): Hadronic Top-jets are constructed taking the Delphes objects which lie outside the HJ ($\Delta R > R$) using Fastjet-3.3.2 with Cambridge-Aachen algorithm, with an initial radius parameter $R' = 1.6$ and $p_T > 200$ GeV. The reconstructed fat-jets are passed through HEPToptagger [169, 170] to identify possible top-jets, with the choice of optimal-R requirement. When a fat-jet is tagged as top-jet, the optimized radius is noted as ‘ R_{opt} ’ for further use. It is to be noted that, for leptonic category, top-jet is not reconstructed due to the presence of neutrino leading to missing momentum.

Other-jets: After HJ and TopJ reconstructions, Delphes objects which are away from HJ and TopJ (i.e, $\Delta R > R, R_{\text{opt}}$) (for leptonic channel, distance from TopJ is not required), are clustered using Anti-kT algorithm with the radius parameter $R''=0.4$ and $p_T > 20$ GeV. The event is accepted if there exists at least one jet. On the other hand, for semi-leptonic final state, jets are matched with the b-quarks after the HJ tagging, to find out remaining b-jets of the event. These b-jets are part of the signal for the semi-leptonic case.

(b) Non-boosted region: In the case of non-boosted region, obviously neither the Higgs nor the top quarks are tagged as fatjet. Instead, using e-flow objects of Delphes, we construct anti-kT jets of radius parameter $R''' = 0.4$ and minimum p_T cut of 20 GeV. Matching these jets with the b-quarks of the event using a matching cone $\Delta R < 0.3$, a set of b-jets are identified.

Higgs-jet(HJ): In order to reconstruct the Higgs boson, the best possible combination of b-like jets are selected by minimizing $(m_{b\bar{b}} - m_H)^2$, where m_H is set to 125 GeV. If $m_{b\bar{b}}$ lies within the mass window $m_H \in [100, 150]$, then the corresponding combination of $b\bar{b}$ system and the invariant mass is assumed to represent the Higgs boson.

Top-jet(TopJ): Out of the remaining set of ordinary jets and the b-jets, the right combination is picked up, which minimizes $(m_{(jjb)} - m_t)^2 + (m_{(jj)} - m_W)^2$, and that represents a top-jet. For the leptonic case, top quark is not fully reconstructed. Instead, the lepton-b system originating from top quark decay is used as a substitute to construct top-quark related observables.

b-jets and other non-b jets: After reconstruction of Higgs boson and top-quark (for hadronic channel) at least one jet (hadronic) or one b-jet and one ordinary jet (leptonic) are required.

Lepton selection : Both leptons (e and μ) are selected with $p_T > 20$ GeV and $|\eta| < 2.5$. The isolation of leptons are ensured using an isolation criteria taking into account the e-flow objects of Delphes as follows,

$$\frac{\sum p_T^{R < r}}{p_{T,\ell}} < I, \quad \ell = e, \mu. \quad (4.4)$$

Here the numerator presents the sum of p_T of all visible collections within a cone of radius R around the lepton, with $r = \frac{10.0}{p_{T,\ell}}$ for boosted category, and $r = 0.3$ for non-boosted category, setting $I = 0.12$ and 0.25 for e and μ respectively. Notably, for the boosted

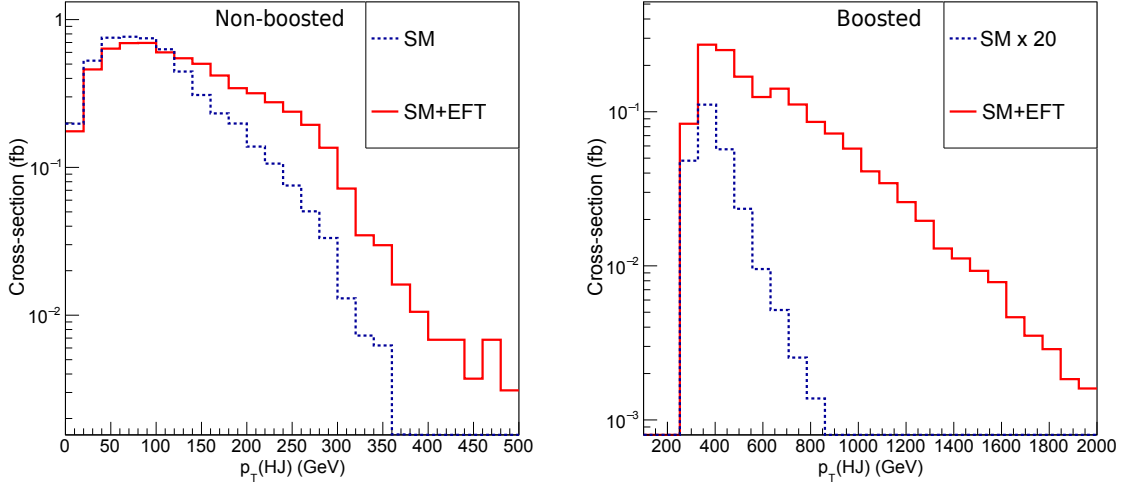


Figure 6: Transverse momentum of the reconstructed Higgs boson (HJ) for non-boosted ($p_T(\text{H}) < 300$ GeV)(left) and boosted region ($p_T(\text{H}) > 300$ GeV)(right) for the hadronic final state.

category, a different isolation procedure with p_T -dependent isolation cone is employed, familiar as mini-isolation [171].

4.2 Results

4.2.1 Effect of SMEFT operators to tHq process

Several kinematic observables are constructed for each case (a) and (b) for “SM+EFT”, setting all WC to their best-fit values. We identify the right set of observables that show a clear deviation at the tail from the SM prediction. In order to quantify the sensitivities, we first estimate the level of contamination due to the SM backgrounds (Eq. 4.3) at the signal region, and then also checked the same including the EFT effects.

We demonstrate the distributions of a few interesting observables for the hadronic (Eq. 4.1) and leptonic final states (4.2), considering both the boosted and non-boosted regions.

- **Hadronic final state:** The cross-section normalized transverse momentum of the reconstructed Higgs boson for boosted (left) and non-boosted (right) cases are presented in Fig. 6. The excess in the p_T spectrum is very large in the case of boosted regime, whereas it is less for the non-boosted case, except beyond the $p_T(\text{H}) > 200$ GeV. The sudden fall, above $p_T(\text{H}) > 300$ GeV is owing to a generator-level cut on the p_T of the Higgs boson. Notice that, for the boosted case, the SM cross-section is multiplied by a factor of 20 for the sake of presentation.

Similarly, the distribution of p_T of the top-jet is shown in Fig. 7 both for SM and SM+EFT cases. As no generator-level selection is imposed on the p_T of the top-quark or the light hard-scattered quark, the distribution in the non-boosted region does not show any

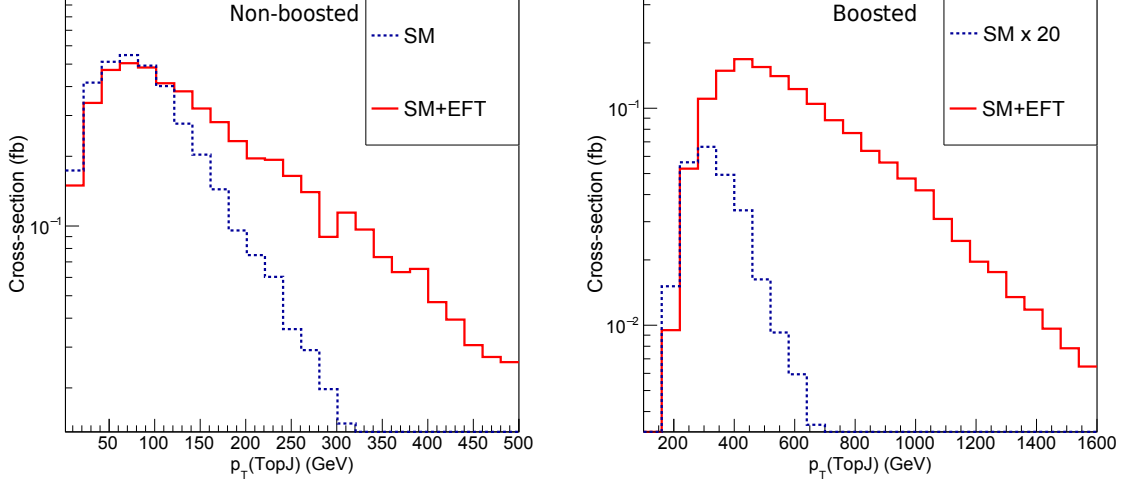


Figure 7: Transverse momentum of the reconstructed Top-jet (TopJ) for the hadronic final state in the same set-up as Fig. 6.

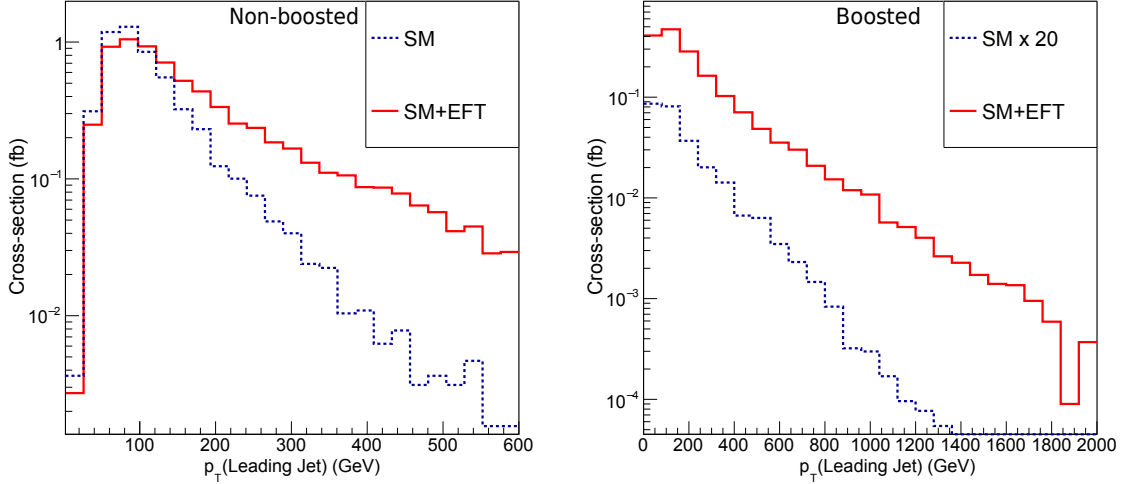


Figure 8: Transverse momentum of the reconstructed leading jet for the hadronic final state in the same set-up as Fig. 6.

abrupt fall as seen before at the higher side of the HJ p_T distribution. In this distribution also, a significant deviation is observed on the higher side, in particular for the boosted case.

The p_T of the leading-jet, as presented in Fig. 8, depicts a mild deviation at the tail, unlike the case of HJ and TopJ. It can be attributed to the fact that the vertex from where the jet originates are not affected by any energy growth due to the scattering sub-amplitude $bW \rightarrow tH$ [122]. The deviations of the TopJ and HJ at the tail of the distributions are

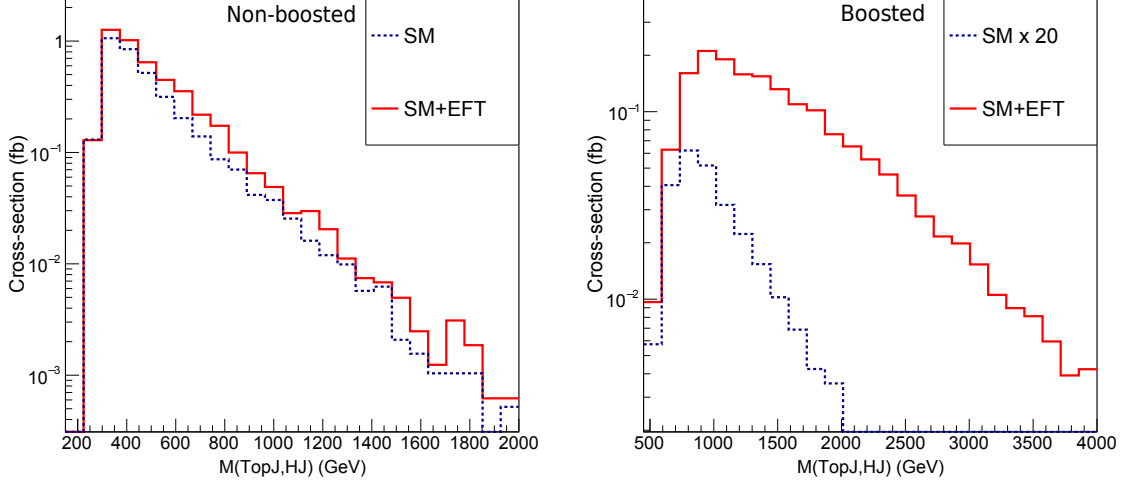


Figure 9: Invariant mass of the Higgs-Jet and Top-jet for the hadronic final state in the same set-up as Fig. 6.

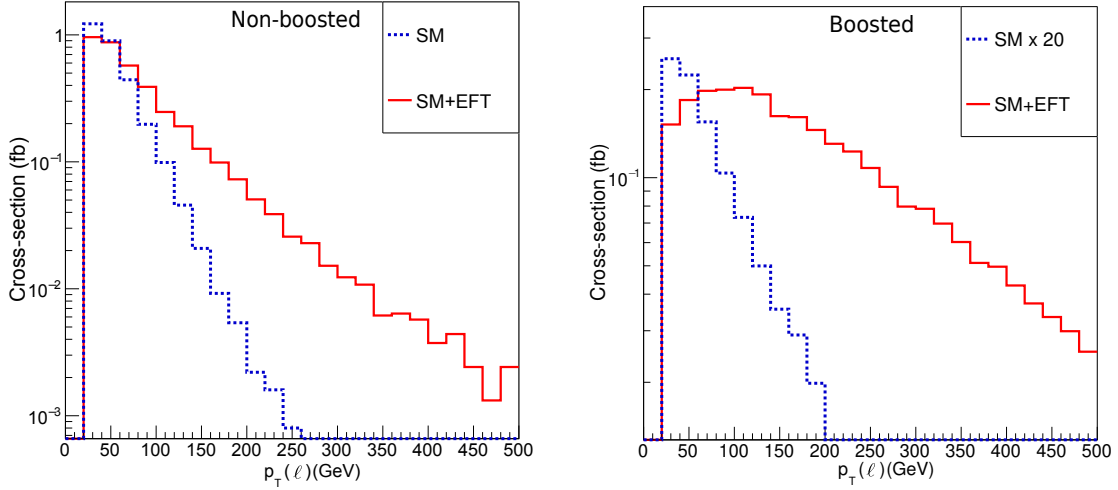


Figure 10: Transverse momentum of the isolated lepton for the leptonic final state in the same set-up as Fig. 6.

also expected to be reflected in the invariant mass of these two objects, as seen in Fig. 9. Remarkably, a very clear deviation is observed, in particular for the boosted case.

- **Leptonic final state:** The distribution of p_T of the lepton arising from the decay of top-quark is presented in Fig. 10. As expected, the lepton receives the similar feature of the p_T of the top, and exhibits substantial deviation as the TopJ. In this case, particularly for the boosted category, the effect is much more pronounced than the p_T of TopJ for hadronic case (Fig. 7).

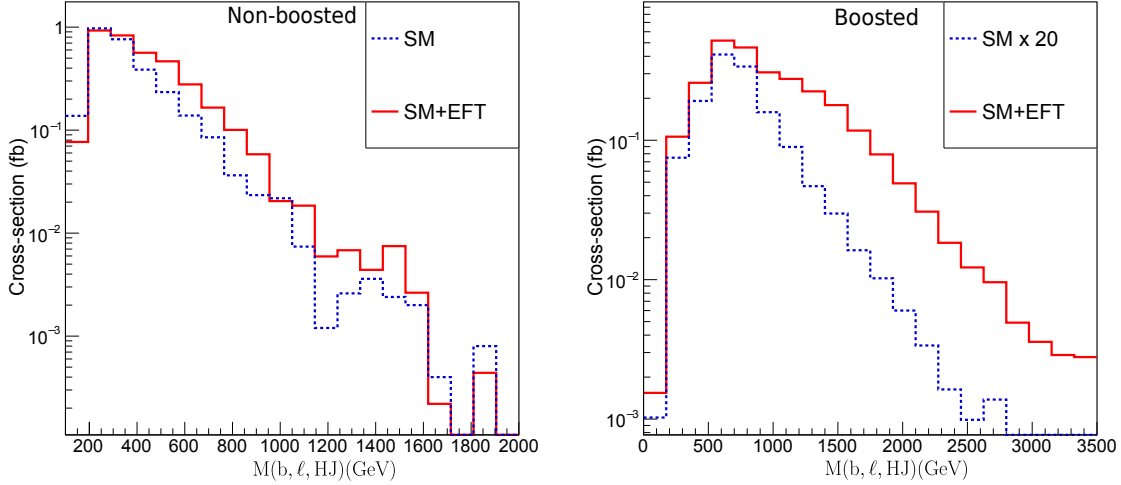


Figure 11: Invariant mass of the lepton, b-jet and Higgs-jet system for the leptonic final state in the same set-up as Fig. 6, requiring $\Delta R(\ell, b) < 1.5$.

Equivalent to the $M(\text{TopJ}, \text{HJ})$ observable for the hadronic case, the invariant mass of the lepton, HJ, and the b-jet is constructed. The b-jets associated with the lepton are identified by requiring the criteria $\Delta R(\ell, b) < 1.5$. In Fig. 11, the invariant mass of b- ℓ -HJ system is presented for the non-boosted (left) and boosted (right) case. Remarkable deviations are observed at the high value of the invariant mass for the boosted case.

4.2.2 Signal and backgrounds

The visible effects of the relevant SMEFT operators in various kinematical observables for the tHq process are presented in the previous section. Deviations from the SM prediction is observed at the tail of the distributions. Discovery potential of the signatures of these operators can be realized once we make a proper estimation of background contamination in the signal regions. The possible dominant sources of SM backgrounds are presented in Eq. 4.3. Now we proceed to find the signal sensitivity, by estimating signal significance for the boosted region of the tHq process.

For the hadronic final state, QCD multi-jet events, having huge cross-section, may add fake contribution as one of the backgrounds. We have checked simulating a sufficient number of QCD events that the contribution is small, though non-negligible compared to the signal in the boosted region with only the minimal selection criteria for the final state Eq. 4.1, and 4.2. However, after implementing other discriminating variables, the QCD contribution is expected to be reduced further and even a multivariate analysis (MVA) may help to bring it down substantially. Due to the lack of appropriate statistics of events after the basic selections, further study turned out to be beyond our scope, and we conclude that the proper estimation of the QCD background is to be done experimentally by a data-driven

Table 12: Signal and background cross-section yields (in fb) for the hadronic final state after basic selections including EFT effects in both cases. The numbers in the parenthesis represent the SM-only background contributions.

	SM+EFT	$t\bar{t}H(b\bar{b})$	$t\bar{t}b\bar{b}$	$t\bar{t}$	$t\bar{t}Z$	$t\bar{t}W$
Cross-section(fb) (LO)	21	21(17)	59(59)	15410(15300)	39(39)	13(13)
No. of HJ =1	9.6	8.5(6.4)	1.3(1.1)	27.8(23.9)	0.7(0.7)	0.08(0.09)
No. of TopJ = 1	1.9	1.3(0.9)	0.2(0.16)	3.0(2.9)	0.08(0.07)	0.005(0.002)
No. of Jets ≥ 1	1.6	1.2(0.9)	0.2(0.15)	2.6(2.5)	0.08(0.06)	0.004(0.001)
$p_T(\text{topJ}) > 400$ GeV	1.3	0.6(0.4)	0.1(0.09)	1.3(1.25)	0.03(0.02)	0.001(0.0008)
$M(\text{topJ, HJ}) > 1000$ GeV	1.1	0.4(0.2)	0.06(0.04)	0.8(0.77)	0.02(0.02)	0.0005(0.0003)

Table 13: Same as in Table 12, but for leptonic final state.

	SM+EFT	$t\bar{t}H(b\bar{b})$	$t\bar{t}b\bar{b}$	$t\bar{t}$	$t\bar{t}Z$	$t\bar{t}W$	$W(\ell\nu)H(b\bar{b})$
Cross-section(fb) (LO)	7	22(17)	59(59)	15480(15300)	39(39)	13(13)	22.2(6.5)
No. of HJ =1	3.5	7.6(6.2)	1.3(1.0)	26.1(23.9)	0.7(0.7)	0.08(0.09)	10.1(2.0)
No. of $\ell = 1$	2.8	2.2(1.8)	0.4(0.3)	6.5(6.2)	0.2(0.2)	0.02(0.03)	8.1(1.6)
No. of Jets ≥ 0	2.8	2.2(1.8)	0.4(0.3)	6.5(6.2)	0.2(0.2)	0.02(0.03)	8.1(1.6)
$p_T(\ell) > 300$ GeV	0.7	0.09(0.06)	0.03(0.01)	0.5(0.3)	0.004(0.002)	0.003(0.002)	1.6(0.1)
$M(\ell, b, \text{HJ}) > 800$ GeV	0.5	0.04(0.03)	0.006(0.004)	0.1(0.08)	0.0003(0.0002)	0.0004(0.0002)	0.8(0.03)

analysis.

The cross-section of each of the background processes at the leading order (LO) are presented in Table 12 and 13, subject to different set of selection cuts as required. For the sake of comparison, the cross-section including EFT (‘SM+EFT’) in the calculation are also presented. Moreover, it is important to note that the SM background processes are simulated including the effect of EFT operators like the signal process, setting the respective WCs to the best-fit values as presented in Table 11. For the background processes, the numbers in the parenthesis represent the cross-section yields due to SM-only contribution, i.e., setting all WCs are zero. The first row presents the fiducial production cross-section at leading order (LO), i.e., subject to the generator-level phase space selections described above, while later rows show the cross-section yields after imposing respective selection cuts.

The reconstruction of one Higgs jet (HJ) in the event is found to be very effective in eliminating an enormous amount of backgrounds, except for $t\bar{t}H$, which includes a true Higgs boson in the final state like the signal. The presence of a single TopJ in the signal also helps in suppressing a substantial fraction of backgrounds owing to the higher top-reconstruction efficiency for the signal, since the population of high p_T top quarks in the signal process is higher compared to the backgrounds. Notably, demanding at least one QCD jet is important to confirm the signal events, although not very effective in reducing the background events. Finally, in order to eliminate further the remaining background yields, a cut on the p_T of the Top-jet and an invariant mass cut of the Top-Higgs system

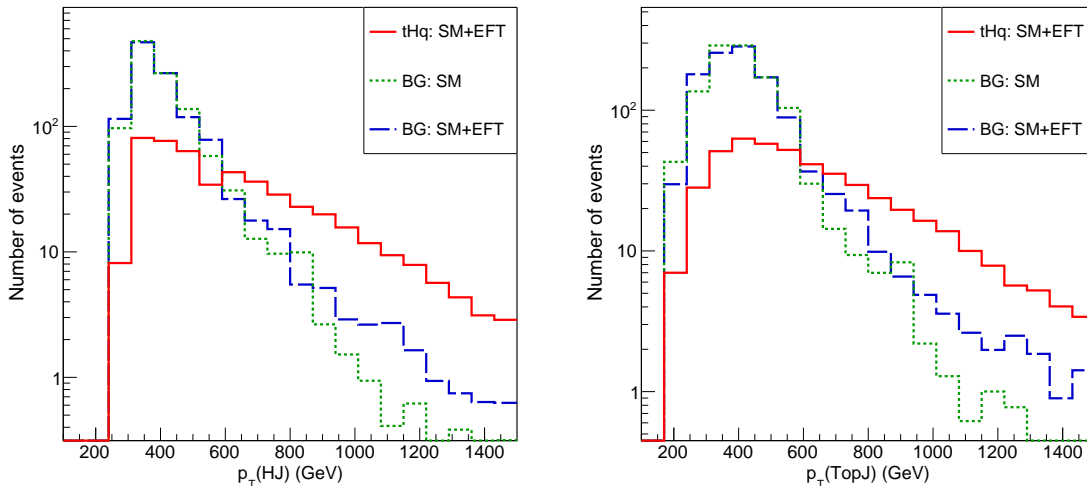


Figure 12: Number of events for $\mathcal{L} = 300 \text{ fb}^{-1}$ in p_T -bins of Higgs-Jet (left) and Top-jet (right) in the boosted region ($p_T(\text{H}) > 300 \text{ GeV}$) of the hadronic final state along with the total main backgrounds. ‘BG’ corresponds to backgrounds, which can either be SM-only or with EFT effects (SM+EFT).

for the hadronic category are imposed. These two cuts essentially isolate the signal region where a substantial excess is visible, in particular, for the boosted case. These two selection cuts reject around 70% or more background events. Similarly, for the leptonic final state, cut on the p_T of lepton followed by a requirement on the invariant mass of the lepton, b, and the HJ system, $M(\ell, b, \text{HJ}) > 800 \text{ GeV}$, eliminate around 99% of backgrounds, without costing too much signal events. The overall acceptance efficiency for the signal is about 5 – 8% for both the hadronic and leptonic categories, whereas, for backgrounds, it is $\sim 0.001\% - 0.006\%$. Finally, the total background cross-section turns out to be $\sim 1.3 \text{ fb}$ and $\sim 0.9 \text{ fb}$ for hadronic and leptonic cases respectively.

The Fig. 12 presents the p_T distribution, normalized to luminosity $\mathcal{L} = 300 \text{ fb}^{-1}$, of TopJ and HJ after all selection cuts for hadronic events. It also shows the clear excess of signal events at the tail. Similarly, for the leptonic category, the distribution of p_T of lepton and invariant mass of lepton, b-jet, and reconstructed Higgs boson are presented in Fig. 13.

The distributions in Fig. 12 and 13 demonstrate that in the boosted region of the tHq production process, a countable excess of events can be observed for a luminosity $\mathcal{L} = 300 \text{ fb}^{-1}$, which is expected to increase by 10 folds for $\mathcal{L} = 3000 \text{ fb}^{-1}$. Alternatively, non-observation of any excess certainly can impose much stronger bounds on the WCs of the relevant operators.

The feature of the ‘high scale sensitivity’ reflected in the excess can be captured in the ‘bin by bin’ estimation of the respective kinematic variable, rather than counting a total

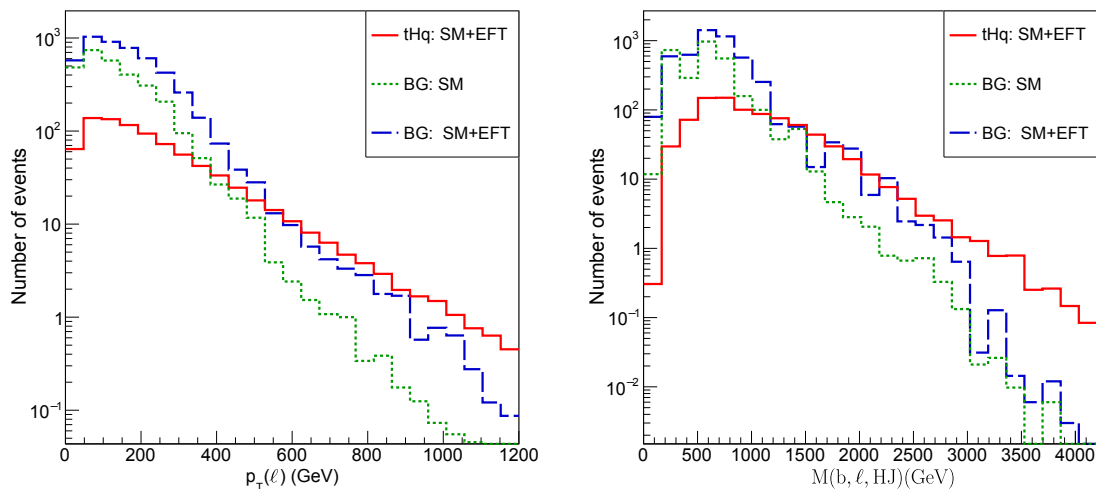


Figure 13: Same as Fig. 12, but in p_T -bins of lepton (left) and invariant mass of Higgs-lepton-bjet system (right) for the leptonic final state.

number of events. Basically, the region where excess is observed is divided into several bins, and the number of events corresponding to those for both the signal and total background is counted. Since p_T of constructed kinematic variables as shown above are expected to be correlated, bins in the 2D plane are considered to be useful in presenting significances. In Fig. 14 we present the signal region in 2D planes dividing into the p_T bins of the HJ and TopJ for hadronic(left) and leptonic(right) case. In each bin, the upper (lower) entries present the signal (total background) yields. The respective colors of each bin show the level of significances, $S/\sqrt{(S+B)}$, for a luminosity option $\mathcal{L} = 300 \text{ fb}^{-1}$.

Notice that for the hadronic case, more than 3σ significance can be achieved for the p_T range 400-1200 GeV of both HJ and TopJ, whereas for the leptonic case, the range appears to be 20-800 GeV for lepton and 400-1200 GeV for HJ. The drop of the signal significance, assuming of 10% background uncertainty, differs from bin to bin with a maximum drop of $\sim 30 - 50\%$ in the lower p_T bins, whereas a negligible reduction (~ 0) towards the higher p_T region. The sensitivity may go up by almost a factor 3 for $\mathcal{L} = 3000 \text{ fb}^{-1}$. Evidently, Fig. 14 demonstrates the discovery potential of the signature of the impact of EFT in tHq process at the LHC. Clearly, presence of EFT effects which is already constrained by the existing data can be found in tHq process even for $\mathcal{L} = 300 \text{ fb}^{-1}$ option at the LHC RUN3 experiment.

5 Summary

We present a detailed study of new physics effects in the single top quark production associated with the SM Higgs boson (tHq) within the SMEFT framework where extra

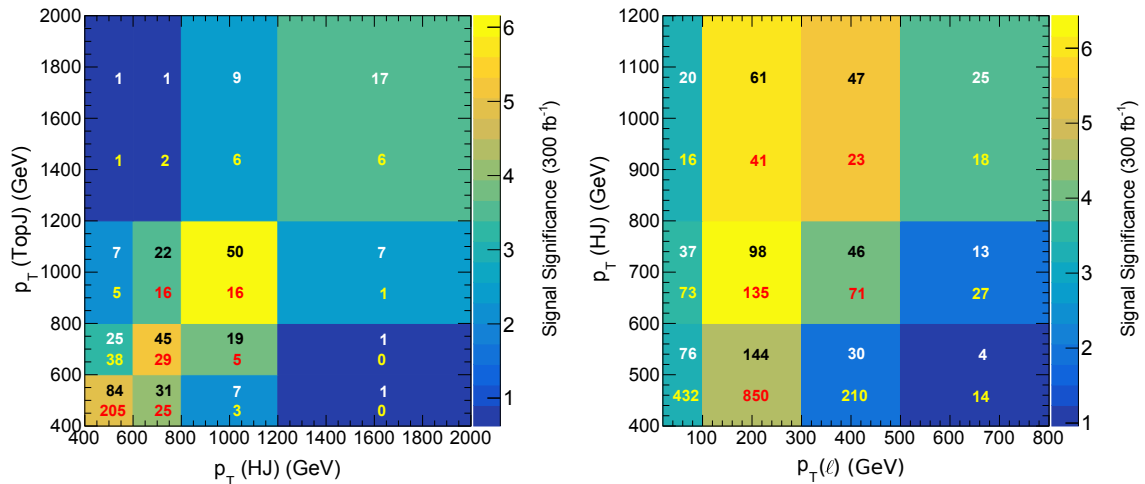


Figure 14: 2D distribution of $p_T(\text{HJ})$ and $p_T(\text{TopJ})$ or $p_T(\ell)$ in terms of signal significance ($S/\sqrt{S+B}$) at $\mathcal{L} = 300 \text{ fb}^{-1}$ for hadronic (left) and leptonic (right) final state. The upper (lower) entries present the number of event yields for signal (total background).

dimension-6 terms are added with the SM lagrangian. As a first step, we isolate a subset of SMEFT operators relevant to the $t\text{H}q$ process using symmetry arguments. The processes involving a top quark and having common interactions with the $t\text{H}q$ are also identified, namely $t\bar{t}H, t\bar{t}H, t\bar{t}W, tZ$ and tj . The total cross-section or differential cross-section, signal strength, etc., are measured for each of these processes at the LHC. The deviation of these latest measurements from the SM prediction are expected to impose constraints on the WCs corresponding to those SMEFT operators involved in the $t\text{H}q$ process. Of course, the sensitivity of the SMEFT operators with the given set of processes determines how strongly those WCs can be constrained. The FIM is constructed in order to have a better quantitative understanding about the level of sensitivity of each of the considered processes on various operators interesting to us. It is also a very useful tool to understand our results qualitatively. The methodology of the evaluation of the tree level cross-sections(LO) for each of the process including SMEFT operators are discussed. The compact analytical form of the total cross-section or any observable can be expressed in terms of a polynomial. The numerical values of the coefficients of the respective SMEFT terms are obtained by fitting the variation of cross-section with the corresponding WC. The constrained ranges of chosen SMEFT operators are obtained following the technique of χ^2 -minimization inputting the measured values along with the uncertainties and the corresponding theoretical predictions of several observables. Eventually, the best fit values of each of these six WCs are presented.

The $t\text{H}q$ process is found to be somewhat special as it incorporates unitarity violating scattering sub-amplitude, namely $bW \rightarrow tH$, resulting in an energy growth, which is

reflected in various kinematic distributions as the excess of events at the tail. This excess of events can be treated as the signature of new physics arising due to the EFT contribution. We perform a dedicated simulation of tHq process at the LHC energy, $\sqrt{s} = 13$ TeV, for both the hadronic and leptonic channels according to the decay of top quark. The simulation is performed categorizing the events into the boosted and non boosted regions, depending on the p_T of the Higgs boson. For the hadronic final state, the signal is characterized by one reconstructed Higgs-jet, one reconstructed Top-jet and at least one extra jet; whereas, for the leptonic final state, an isolated lepton and an extra b-jet is selected instead of a Top-jet. While in the non-boosted scenario, defined by $p_T(\text{H}) < 300$ GeV, EFT effects in different distributions are found to be small compared to the SM distributions. In contrast, these effects turn out to be huge in the boosted region ($p_T(\text{H}) > 300$ GeV).

Having these interesting observations, we concentrate on the boosted region to find the discovery potential of the EFT effects. A detailed simulation of backgrounds are performed to find the signal significance. It is to be noted that the backgrounds are also simulated including the contributions of SMEFT operators. Systematically selection cuts are applied to suppress backgrounds without costing signal significantly. Instead of counting total number of excess events in the signal region after background rejection, we present it in bins of a few interesting observables. For hadronic case, the significances are presented in the p_T bins of Higgs and Top jets whereas for leptonic case, p_T of Higgs jet and lepton are considered. The p_T -binned analysis turns out to be very effective to single out excesses at the tails of the distributions. It is seen that, a reasonable signal significance $\sim 5\sigma$ can be achieved in most of the higher p_T -bins at the high luminosity option $\mathcal{L} = 300 \text{ fb}^{-1}$, presumably which will further increase at HL-LHC option $\mathcal{L} = 3000 \text{ fb}^{-1}$. In conclusion, our analysis shows that, the scope of the tHq process in boosted scenario is very promising in order to observe discoverable excess due to EFT effects. A more systematic simulation using the p-p collision data can reveal the existence of SMEFT effects, if exist, in the tHq process. We would like to draw the attention of our experimental colleagues in this regard. However, the non-observation of any effect can put severe constraints on the relevant sensitive operators considered in this study.

Acknowledgments

Authors are thankful to Prof. Fabio Maltoni and Prof. Carlos Wagner for valuable suggestions and also to Dr. Suman Chatterjee, Dr. Saikat Karmakar, Dr. Ken Mimasu and Kelci Mohrman for useful discussions. AR also acknowledges High-Performance Computing facility at TIFR for making high volume of computations possible and ‘Infosys-TIFR Leading Edge Travel Grant’ for providing support to present this study at the ICHEP, 6-13th July 2022, held at Bologna, Italy.

A Signal strength in terms of WCs including EFT

The signal strength (μ) of any given process can be split into the production and decay part, and the decay part is expressed in terms of the decay widths of the final state particles. As an example, we have considered here the decay of the Higgs boson. But, in general, the decay of any particle, such as the top quark or Z boson, etc. can be considered.

$$\begin{aligned}\mu_{xx}^{th} &= \frac{\sigma^{EFT}(pp \rightarrow h)}{\sigma^{SM}(pp \rightarrow h)} \times \left(\frac{\Gamma_x^{EFT}(c_i)}{\Gamma_x^{SM}} \right) \times \left(\frac{\Gamma_{tot}^{EFT}(c_i)}{\Gamma_{tot}^{SM}} \right)^{-1} \\ &= \frac{\sigma^{EFT}}{\sigma^{SM}} \times \left(\frac{\Gamma_x^{EFT}(c_i)}{\Gamma_x^{SM}} \right) \times \left(\frac{\sum_y \Gamma_y^{EFT}(c_i)}{\sum_z \Gamma_z^{SM}} \right)^{-1}\end{aligned}\quad (\text{A.1})$$

where x, y, z are possible final states.

In the framework of EFT expansion, using Eq. 3.2, we can write both the production cross-section and decay width in the following form,

$$\sigma^{EFT}(\vec{C}) = \sigma^{SM} + \sum_{i=1}^n a_i^\sigma c_i + \sum_{i \leq j} b_{ij}^\sigma c_i c_j, \quad (\text{A.2})$$

$$\Gamma_x^{EFT}(\vec{C}) = \Gamma_x^{SM} + \sum_{i=1}^n a_i^\Gamma c_i + \sum_{i \leq j} b_{ij}^\Gamma c_i c_j, \quad (\text{A.3})$$

where, a_i^σ and b_{ij}^σ are polynomial coefficients for production, while a_i^Γ and b_{ij}^Γ are those for decay width. Using Eq. 3.4, A.2 and A.3 one can write,

$$\begin{aligned}\mu_{xx}^{th}(\vec{C}) &= \left(\frac{\sigma^{SM} + \sum_{i=1}^N a_i^\sigma c_i + \sum_{j \leq k} b_{jk}^\sigma c_j c_k}{\sigma^{SM}} \right) \times \left(\frac{\Gamma_x^{SM} + \sum_{l=1}^N a_l^\Gamma c_l + \sum_{m \leq n} b_{mn}^\Gamma c_m c_n}{\Gamma_x^{SM}} \right) \\ &\quad \times \left(\frac{\sum_y \left(\Gamma_y^{SM} + \sum_{r=1}^N a_r^\Gamma c_r + \sum_{s \leq t} b_{st}^\Gamma c_s c_t \right)}{\sum_y \Gamma_z^{SM}} \right) \\ &= \left(1 + \sum_i \left(\frac{a_i^\sigma}{\sigma^{SM}} \right) c_i + \sum_{j \leq k} \left(\frac{b_{jk}^\sigma}{\sigma^{SM}} \right) c_j c_k \right) \times \left(1 + \sum_l \left(\frac{a_l^\Gamma}{\Gamma_x^{SM}} \right) c_l + \sum_{m \leq n} \left(\frac{b_{mn}^\Gamma}{\Gamma_x^{SM}} \right) c_m c_n \right) \\ &\quad \times \left(\sum_y \left[\frac{\Gamma_y^{SM}}{\Gamma_{tot}^{SM}} + \sum_r \left(\frac{a_r^\Gamma}{\Gamma_{tot}^{SM}} \right) c_r + \sum_{s \leq t} \left(\frac{b_{st}^\Gamma}{\Gamma_{tot}^{SM}} \right) c_s c_t \right] \right)^{-1} \\ &= \left(1 + \sum_i \left(\frac{a_i^\sigma}{\sigma^{SM}} \right) c_i + \sum_{j \leq k} \left(\frac{b_{jk}^\sigma}{\sigma^{SM}} \right) c_j c_k \right) \times \left(1 + \sum_l \left(\frac{a_l^\Gamma}{\Gamma_x^{SM}} \right) c_l + \sum_{m \leq n} \left(\frac{b_{mn}^\Gamma}{\Gamma_x^{SM}} \right) c_m c_n \right) \\ &\quad \times \left(1 - \sum_y \left[\sum_r \left(\frac{a_r^\Gamma}{\Gamma_{tot}^{SM}} \right) c_r + \sum_{s \leq t} \left(\frac{b_{st}^\Gamma}{\Gamma_{tot}^{SM}} \right) c_s c_t \right] \right)\end{aligned}$$

$$\begin{aligned}
&= 1 + \sum_i c_i \left[\frac{a_i^\sigma}{\sigma^{SM}} + \frac{a_i^{\Gamma_x}}{\Gamma_x^{SM}} - \sum_y \left(\frac{a_i^{\Gamma_y}}{\Gamma_{tot}^{SM}} \right) \right] + \sum_{j \leq k} c_j c_k \left[\left(\frac{a_j^\sigma a_k^{\Gamma_x}}{\sigma^{SM} \Gamma_x^{SM}} \right) - \sum_y \left(\frac{a_j^\sigma a_k^{\Gamma_y}}{\sigma^{SM} \Gamma_{tot}^{SM}} \right) \right. \\
&\quad \left. - \sum_y \left(\frac{a_j^{\Gamma_x} a_k^{\Gamma_y}}{\Gamma_x^{SM} \Gamma_{tot}^{SM}} \right) + \frac{b_{jk}^\sigma}{\sigma^{SM}} + \frac{b_{jk}^{\Gamma_x}}{\Gamma_x^{SM}} - \sum_y \left(\frac{b_{jk}^{\Gamma_y}}{\Gamma_{tot}^{SM}} \right) \right] \\
&= 1 + \sum_i A_i c_i + \sum_{j \leq k} B_{jk} c_j c_k. \tag{A.4}
\end{aligned}$$

Where,

$$A_i = \frac{a_i^\sigma}{\sigma^{SM}} + \frac{a_i^{\Gamma_x}}{\Gamma_x^{SM}} - \sum_y \left(\frac{a_i^{\Gamma_y}}{\Gamma_{tot}^{SM}} \right) \tag{A.5}$$

$$B_{jk} = \left(\frac{a_j^\sigma a_k^{\Gamma_x}}{\sigma^{SM} \Gamma_x^{SM}} \right) - \sum_y \left(\frac{a_j^\sigma a_k^{\Gamma_y}}{\sigma^{SM} \Gamma_{tot}^{SM}} \right) - \sum_y \left(\frac{a_j^{\Gamma_x} a_k^{\Gamma_y}}{\Gamma_x^{SM} \Gamma_{tot}^{SM}} \right) + \frac{b_{jk}^\sigma}{\sigma^{SM}} + \frac{b_{jk}^{\Gamma_x}}{\Gamma_x^{SM}} - \sum_y \left(\frac{b_{jk}^{\Gamma_y}}{\Gamma_{tot}^{SM}} \right) \tag{A.6}$$

References

- [1] T. Appelquist and J. Carazzone, *Infrared Singularities and Massive Fields*, *Phys. Rev. D* **11** (1975) 2856.
- [2] S. Weinberg, *Baryon and Lepton Nonconserving Processes*, *Phys. Rev. Lett.* **43** (1979) 1566.
- [3] H.A. Weldon and A. Zee, *Operator Analysis of New Physics*, *Nucl. Phys. B* **173** (1980) 269.
- [4] E. Eichten, K.D. Lane and M.E. Peskin, *New Tests for Quark and Lepton Substructure*, *Phys. Rev. Lett.* **50** (1983) 811.
- [5] I. Brivio and M. Trott, *The Standard Model as an Effective Field Theory*, *Phys. Rept.* **793** (2019) 1 [1706.08945].
- [6] W. Buchmuller and D. Wyler, *Effective Lagrangian Analysis of New Interactions and Flavor Conservation*, *Nucl. Phys. B* **268** (1986) 621.
- [7] B. Grzadkowski, M. Iskrzynski, M. Misiak and J. Rosiek, *Dimension-Six Terms in the Standard Model Lagrangian*, *JHEP* **10** (2010) 085 [1008.4884].
- [8] C. Leung, S. Love and S. Rao, *Low-energy manifestations of a new interactions scale: Operator analysis*, *Zeitschrift für Physik C* **31** (1986) 433.
- [9] O. Bessidskaia Bylund, F. Maltoni, I. Tsirikos, E. Vryonidou and C. Zhang, *Probing top quark neutral couplings in the Standard Model Effective Field Theory at NLO in QCD*, *JHEP* **05** (2016) 052 [1601.08193].
- [10] S. Dawson, P.P. Giardino and A. Ismail, *Standard model EFT and the Drell-Yan process at high energy*, *Phys. Rev. D* **99** (2019) 035044 [1811.12260].
- [11] Q.-Y. Hu, X.-Q. Li and Y.-D. Yang, *$b \rightarrow c\tau\nu$ transitions in the standard model effective field theory*, *Eur. Phys. J. C* **79** (2019) 264 [1810.04939].
- [12] J. D’Hondt, A. Mariotti, K. Mimasu, S. Moortgat and C. Zhang, *Learning to pinpoint effective operators at the LHC: a study of the $t\bar{t}b\bar{b}$ signature*, *JHEP* **11** (2018) 131 [1807.02130].

- [13] C. Degrande, F. Maltoni, K. Mimasu, E. Vryonidou and C. Zhang, *Single-top associated production with a Z or H boson at the LHC: the SMEFT interpretation*, *JHEP* **10** (2018) 005 [[1804.07773](#)].
- [14] S. Dawson, S. Homiller and S.D. Lane, *Putting standard model EFT fits to work*, *Phys. Rev. D* **102** (2020) 055012 [[2007.01296](#)].
- [15] R. Goldouzian and M.D. Hildreth, *LHC dijet angular distributions as a probe for the dimension-six triple gluon vertex*, *Phys. Lett. B* **811** (2020) 135889 [[2001.02736](#)].
- [16] J. Aebischer, W. Dekens, E.E. Jenkins, A.V. Manohar, D. Sengupta and P. Stoffer, *Effective field theory interpretation of lepton magnetic and electric dipole moments*, *JHEP* **07** (2021) 107 [[2102.08954](#)].
- [17] J.J. Ethier, R. Gomez-Ambrosio, G. Magni and J. Rojo, *SMEFT analysis of vector boson scattering and diboson data from the LHC Run II*, *Eur. Phys. J. C* **81** (2021) 560 [[2101.03180](#)].
- [18] S. Khatibi and H. Khanpour, *Probing four-fermion operators in the triple top production at future hadron colliders*, *Nucl. Phys. B* **967** (2021) 115432 [[2011.15060](#)].
- [19] J.Y. Araz, S. Banerjee, R.S. Gupta and M. Spannowsky, *Precision SMEFT bounds from the VBF Higgs at high transverse momentum*, *JHEP* **04** (2021) 125 [[2011.03555](#)].
- [20] R. Boughezal, C.-Y. Chen, F. Petriello and D. Wiegand, *Four-lepton Z boson decay constraints on the standard model EFT*, *Phys. Rev. D* **103** (2021) 055015 [[2010.06685](#)].
- [21] R. Boughezal, E. Mereghetti and F. Petriello, *Dilepton production in the SMEFT at $O(1/\Lambda^4)$* , *Phys. Rev. D* **104** (2021) 095022 [[2106.05337](#)].
- [22] M. Battaglia, M. Grazzini, M. Spira and M. Wiesemann, *Sensitivity to BSM effects in the Higgs p_T spectrum within SMEFT*, *JHEP* **11** (2021) 173 [[2109.02987](#)].
- [23] R. Bellan et al., *A sensitivity study of VBS and diboson WW to dimension-6 EFT operators at the LHC*, *JHEP* **05** (2022) 039 [[2108.03199](#)].
- [24] Y. Afik, S. Bar-Shalom, K. Pal, A. Soni and J. Wudka, *Multi-lepton probes of new physics and lepton-universality in top-quark interactions*, *Nucl. Phys. B* **980** (2022) 115849 [[2111.13711](#)].
- [25] H.E. Faham, F. Maltoni, K. Mimasu and M. Zaro, *Single top production in association with a WZ pair at the LHC in the SMEFT*, *JHEP* **01** (2022) 100 [[2111.03080](#)].
- [26] S. Dawson, S. Homiller and M. Sullivan, *Impact of dimension-eight SMEFT contributions: A case study*, *Phys. Rev. D* **104** (2021) 115013 [[2110.06929](#)].
- [27] J. Ellis, S.-F. Ge and K. Ma, *Hadron collider probes of the quartic couplings of gluons to the photon and Z boson*, *JHEP* **04** (2022) 123 [[2112.06729](#)].
- [28] L. Allwicher, D.A. Faroughy, F. Jaffredo, O. Sumensari and F. Wilsch, *Drell-Yan Tails Beyond the Standard Model*, [2207.10714](#).
- [29] R. Boughezal, Y. Huang and F. Petriello, *Exploring the SMEFT at dimension-8 with Drell-Yan transverse momentum measurements*, [2207.01703](#).

- [30] R.K. Barman and A. Ismail, *Constraining the top electroweak sector of the SMEFT through Z associated top pair and single top production at the HL-LHC*, [2205.07912](#).
- [31] U. Haisch, D.J. Scott, M. Wiesemann, G. Zanderighi and S. Zanolini, *NNLO event generation for $pp \rightarrow Zh \rightarrow \ell^+ \ell^- b\bar{b}$ production in the SM effective field theory*, *JHEP* **07** (2022) 054 [[2204.00663](#)].
- [32] T. Kim and A. Martin, *Monolepton production in SMEFT to $\mathcal{O}(1/\Lambda^4)$ and beyond*, [2203.11976](#).
- [33] R. Goldouzian, J.H. Kim, K. Lannon, A. Martin, K. Mohrman and A. Wightman, *Matching in $pp \rightarrow t\bar{t}W/Z/h + \text{jet}$ SMEFT studies*, *JHEP* **06** (2021) 151 [[2012.06872](#)].
- [34] Z. Han and W. Skiba, *Effective theory analysis of precision electroweak data*, *Phys. Rev. D* **71** (2005) 075009 [[hep-ph/0412166](#)].
- [35] T. Corbett, O.J.P. Eboli, J. Gonzalez-Fraile and M.C. Gonzalez-Garcia, *Robust Determination of the Higgs Couplings: Power to the Data*, *Phys. Rev. D* **87** (2013) 015022 [[1211.4580](#)].
- [36] W.-F. Chang, W.-P. Pan and F. Xu, *Effective gauge-Higgs operators analysis of new physics associated with the Higgs boson*, *Phys. Rev. D* **88** (2013) 033004 [[1303.7035](#)].
- [37] T. Corbett, O.J.P. Éboli, J. Gonzalez-Fraile and M.C. Gonzalez-Garcia, *Determining Triple Gauge Boson Couplings from Higgs Data*, *Phys. Rev. Lett.* **111** (2013) 011801 [[1304.1151](#)].
- [38] B. Dumont, S. Fichet and G. von Gersdorff, *A Bayesian view of the Higgs sector with higher dimensional operators*, *JHEP* **07** (2013) 065 [[1304.3369](#)].
- [39] A. Pomarol and F. Riva, *Towards the Ultimate SM Fit to Close in on Higgs Physics*, *JHEP* **01** (2014) 151 [[1308.2803](#)].
- [40] J. Elias-Miro, J.R. Espinosa, E. Masso and A. Pomarol, *Higgs windows to new physics through $d=6$ operators: constraints and one-loop anomalous dimensions*, *JHEP* **11** (2013) 066 [[1308.1879](#)].
- [41] E. Boos, V. Bunichev, M. Dubinin and Y. Kurihara, *Higgs boson signal at complete tree level in the SM extension by dimension-six operators*, *Phys. Rev. D* **89** (2014) 035001 [[1309.5410](#)].
- [42] J. Ellis, V. Sanz and T. You, *Complete Higgs Sector Constraints on Dimension-6 Operators*, *JHEP* **07** (2014) 036 [[1404.3667](#)].
- [43] J. Ellis, V. Sanz and T. You, *The Effective Standard Model after LHC Run I*, *JHEP* **03** (2015) 157 [[1410.7703](#)].
- [44] A. Falkowski and F. Riva, *Model-independent precision constraints on dimension-6 operators*, *JHEP* **02** (2015) 039 [[1411.0669](#)].
- [45] A. Efrati, A. Falkowski and Y. Soreq, *Electroweak constraints on flavorful effective theories*, *JHEP* **07** (2015) 018 [[1503.07872](#)].
- [46] A. Falkowski and K. Mimouni, *Model independent constraints on four-lepton operators*, *JHEP* **02** (2016) 086 [[1511.07434](#)].

- [47] A. Buckley, C. Englert, J. Ferrando, D.J. Miller, L. Moore, M. Russell et al., *Constraining top quark effective theory in the LHC Run II era*, *JHEP* **04** (2016) 015 [[1512.03360](#)].
- [48] L. Berthier, M. Bjørn and M. Trott, *Incorporating doubly resonant W^\pm data in a global fit of SMEFT parameters to lift flat directions*, *JHEP* **09** (2016) 157 [[1606.06693](#)].
- [49] A. Falkowski, M. González-Alonso and K. Mimouni, *Compilation of low-energy constraints on 4-fermion operators in the SMEFT*, *JHEP* **08** (2017) 123 [[1706.03783](#)].
- [50] J. Ellis, C.W. Murphy, V. Sanz and T. You, *Updated Global SMEFT Fit to Higgs, Diboson and Electroweak Data*, *JHEP* **06** (2018) 146 [[1803.03252](#)].
- [51] S. Banerjee, C. Englert, R.S. Gupta and M. Spannowsky, *Probing Electroweak Precision Physics via boosted Higgs-strahlung at the LHC*, *Phys. Rev. D* **98** (2018) 095012 [[1807.01796](#)].
- [52] E. da Silva Almeida, A. Alves, N. Rosa Agostinho, O.J.P. Éboli and M.C. Gonzalez-Garcia, *Electroweak Sector Under Scrutiny: A Combined Analysis of LHC and Electroweak Precision Data*, *Phys. Rev. D* **99** (2019) 033001 [[1812.01009](#)].
- [53] J. Aebischer, J. Kumar, P. Stangl and D.M. Straub, *A Global Likelihood for Precision Constraints and Flavour Anomalies*, *Eur. Phys. J. C* **79** (2019) 509 [[1810.07698](#)].
- [54] A. Biekötter, T. Corbett and T. Plehn, *The Gauge-Higgs Legacy of the LHC Run II*, *SciPost Phys.* **6** (2019) 064 [[1812.07587](#)].
- [55] S. Descotes-Genon, A. Falkowski, M. Fedele, M. González-Alonso and J. Virto, *The CKM parameters in the SMEFT*, *JHEP* **05** (2019) 172 [[1812.08163](#)].
- [56] L. Silvestrini and M. Valli, *Model-independent Bounds on the Standard Model Effective Theory from Flavour Physics*, *Phys. Lett. B* **799** (2019) 135062 [[1812.10913](#)].
- [57] N.P. Hartland, F. Maltoni, E.R. Nocera, J. Rojo, E. Slade, E. Vryonidou et al., *A Monte Carlo global analysis of the Standard Model Effective Field Theory: the top quark sector*, *JHEP* **04** (2019) 100 [[1901.05965](#)].
- [58] T. Hurth, S. Renner and W. Shepherd, *Matching for FCNC effects in the flavour-symmetric SMEFT*, *JHEP* **06** (2019) 029 [[1903.00500](#)].
- [59] S. van Beek, E.R. Nocera, J. Rojo and E. Slade, *Constraining the SMEFT with Bayesian reweighting*, *SciPost Phys.* **7** (2019) 070 [[1906.05296](#)].
- [60] G. Durieux, A. Irlès, V. Miralles, A. Peñuelas, R. Pöschl, M. Perelló et al., *The electro-weak couplings of the top and bottom quarks — Global fit and future prospects*, *JHEP* **12** (2019) 98 [[1907.10619](#)].
- [61] S. Bickmann, J. Erdmann, C. Grunwald, G. Hiller and K. Kröninger, *Constraining top-quark couplings combining top-quark and B decay observables*, *Eur. Phys. J. C* **80** (2020) 136 [[1909.13632](#)].
- [62] I. Brivio, S. Bruggisser, F. Maltoni, R. Moutafis, T. Plehn, E. Vryonidou et al., *O new physics, where art thou? A global search in the top sector*, *JHEP* **02** (2020) 131 [[1910.03606](#)].

- [63] A. Falkowski and D. Straub, *Flavourful SMEFT likelihood for Higgs and electroweak data*, *JHEP* **04** (2020) 066 [[1911.07866](#)].
- [64] S. Banerjee, R.S. Gupta, J.Y. Reiness, S. Seth and M. Spannowsky, *Towards the ultimate differential SMEFT analysis*, *JHEP* **09** (2020) 170 [[1912.07628](#)].
- [65] CMS collaboration, *Using associated top quark production to probe for new physics within the framework of effective field theory*, .
- [66] ATLAS collaboration, *Interpretations of the combined measurement of Higgs boson production and decay*, .
- [67] CMS collaboration, *Combined Higgs boson production and decay measurements with up to 137 fb^{-1} of proton-proton collision data at $\sqrt{s} = 13 \text{ TeV}$* , .
- [68] R. Aoude, T. Hurth, S. Renner and W. Shepherd, *The impact of flavour data on global fits of the MFV SMEFT*, *JHEP* **12** (2020) 113 [[2003.05432](#)].
- [69] A. Biekötter, R. Gomez-Ambrosio, P. Gregg, F. Krauss and M. Schönherr, *Constraining SMEFT operators with associated $h\gamma$ production in weak boson fusion*, *Phys. Lett. B* **814** (2021) 136079 [[2003.06379](#)].
- [70] D.A. Faroughy, G. Isidori, F. Wilsch and K. Yamamoto, *Flavour symmetries in the SMEFT*, *JHEP* **08** (2020) 166 [[2005.05366](#)].
- [71] J. Aebischer and J. Kumar, *Flavour violating effects of Yukawa running in SMEFT*, *JHEP* **09** (2020) 187 [[2005.12283](#)].
- [72] J. Aebischer, C. Bobeth, A.J. Buras and J. Kumar, *SMEFT ATLAS of $\Delta F = 2$ transitions*, *JHEP* **12** (2020) 187 [[2009.07276](#)].
- [73] A. Falkowski, M. González-Alonso and O. Naviliat-Cuncic, *Comprehensive analysis of beta decays within and beyond the Standard Model*, *JHEP* **04** (2021) 126 [[2010.13797](#)].
- [74] A. Falkowski, S. Ganguly, P. Gras, J.M. No, K. Tobioka, N. Vignaroli et al., *Light quark Yukawas in triboson final states*, *JHEP* **04** (2021) 023 [[2011.09551](#)].
- [75] J. Ellis, M. Madigan, K. Mimasu, V. Sanz and T. You, *Top, Higgs, Diboson and Electroweak Fit to the Standard Model Effective Field Theory*, *JHEP* **04** (2021) 279 [[2012.02779](#)].
- [76] SMEFT collaboration, *Combined SMEFT interpretation of Higgs, diboson, and top quark data from the LHC*, *JHEP* **11** (2021) 089 [[2105.00006](#)].
- [77] ATLAS collaboration, *Search for flavour-changing neutral current top-quark decays $t \rightarrow qZ$ in proton-proton collisions at $\sqrt{s} = 13 \text{ TeV}$ with the ATLAS detector*, *JHEP* **07** (2018) 176 [[1803.09923](#)].
- [78] ATLAS collaboration, *Search for flavour-changing neutral currents in processes with one top quark and a photon using 81 fb^{-1} of pp collisions at $\sqrt{s} = 13 \text{ TeV}$ with the ATLAS experiment*, *Phys. Lett. B* **800** (2020) 135082 [[1908.08461](#)].
- [79] ATLAS collaboration, *Measurement of the $t\bar{t}Z$ and $t\bar{t}W$ cross sections in proton-proton collisions at $\sqrt{s} = 13 \text{ TeV}$ with the ATLAS detector*, *Phys. Rev. D* **99** (2019) 072009 [[1901.03584](#)].

- [80] ATLAS collaboration, *Higgs boson production cross-section measurements and their EFT interpretation in the 4ℓ decay channel at $\sqrt{s}=13$ TeV with the ATLAS detector*, *Eur. Phys. J. C* **80** (2020) 957 [[2004.03447](#)].
- [81] ATLAS collaboration, *Combined effective field theory interpretation of $H \rightarrow WW^*$ and WW measurements using ATLAS data*, .
- [82] ATLAS collaboration, *Measurements of differential cross-sections in four-lepton events in 13 TeV proton-proton collisions with the ATLAS detector*, *JHEP* **07** (2021) 005 [[2103.01918](#)].
- [83] ATLAS collaboration, *Measurement of the energy asymmetry in $t\bar{t}j$ production at 13 TeV with the ATLAS experiment and interpretation in the SMEFT framework*, *Eur. Phys. J. C* **82** (2022) 374 [[2110.05453](#)].
- [84] ATLAS collaboration, *Measurement of the polarisation of single top quarks and antiquarks produced in the t -channel at $\sqrt{s} = 13$ TeV and bounds on the tWb dipole operator from the ATLAS experiment*, [2202.11382](#).
- [85] ATLAS collaboration, *Measurements of differential cross-sections in top-quark pair events with a high transverse momentum top quark and limits on beyond the Standard Model contributions to top-quark pair production with the ATLAS detector at $\sqrt{s} = 13$ TeV*, *JHEP* **06** (2022) 063 [[2202.12134](#)].
- [86] ATLAS collaboration, *Search for flavor-changing neutral-current couplings between the top quark and the Z boson with LHC Run2 proton-proton collisions at $\sqrt{s} = 13$ TeV with the ATLAS detector*, .
- [87] ATLAS collaboration, *Differential $t\bar{t}$ cross-section measurements using boosted top quarks in the all-hadronic final state with 139 fb^{-1} of ATLAS data*, .
- [88] ATLAS collaboration, *Differential $t\bar{t}$ cross-section measurements using boosted top quarks in the all-hadronic final state with 139 fb^{-1} of ATLAS data*, [2205.02817](#).
- [89] ATLAS collaboration, *Measurement of the properties of Higgs boson production at $\sqrt{s} = 13$ TeV in the $H \rightarrow \gamma\gamma$ channel using 139 fb^{-1} of pp collision data with the ATLAS experiment*, [2207.00348](#).
- [90] CMS collaboration, *Search for new physics in top quark production in dilepton final states in proton-proton collisions at $\sqrt{s} = 13$ TeV*, *Eur. Phys. J. C* **79** (2019) 886 [[1903.11144](#)].
- [91] CMS collaboration, *Measurement of the top quark polarization and $t\bar{t}$ spin correlations using dilepton final states in proton-proton collisions at $\sqrt{s} = 13$ TeV*, *Phys. Rev. D* **100** (2019) 072002 [[1907.03729](#)].
- [92] CMS collaboration, *Search for the production of four top quarks in the single-lepton and opposite-sign dilepton final states in proton-proton collisions at $\sqrt{s} = 13$ TeV*, *JHEP* **11** (2019) 082 [[1906.02805](#)].
- [93] CMS collaboration, *Measurement of top quark pair production in association with a Z boson in proton-proton collisions at $\sqrt{s} = 13$ TeV*, *JHEP* **03** (2020) 056 [[1907.11270](#)].
- [94] CMS collaboration, *Search for new physics in top quark production with additional leptons*

- in proton-proton collisions at $\sqrt{s} = 13$ TeV using effective field theory, *JHEP* **03** (2021) 095 [[2012.04120](#)].
- [95] CMS collaboration, *Constraints on anomalous Higgs boson couplings to vector bosons and fermions in its production and decay using the four-lepton final state*, *Phys. Rev. D* **104** (2021) 052004 [[2104.12152](#)].
- [96] CMS collaboration, *Probing effective field theory operators in the associated production of top quarks with a Z boson in multilepton final states at $\sqrt{s} = 13$ TeV*, *JHEP* **12** (2021) 083 [[2107.13896](#)].
- [97] CMS collaboration, *Measurement of the inclusive and differential $t\bar{t}\gamma$ cross section and EFT interpretation in the dilepton channel at $\sqrt{s} = 13$ TeV*, .
- [98] CMS collaboration, *Measurement and QCD analysis of double-differential inclusive jet cross sections in proton-proton collisions at $\sqrt{s} = 13$ TeV*, *JHEP* **02** (2022) 142 [[2111.10431](#)].
- [99] F. Bezrukov and M. Shaposhnikov, *Why should we care about the top quark Yukawa coupling?*, *J. Exp. Theor. Phys.* **120** (2015) 335 [[1411.1923](#)].
- [100] M. Carena, M. Olechowski, S. Pokorski and C. Wagner, *Radiative electroweak symmetry breaking and the infrared fixed point of the top quark mass*, *Nuclear Physics B* **419** (1994) 213.
- [101] D. Delepine, J.M. Gerard and R. Gonzalez Felipe, *Is the standard Higgs scalar elementary?*, *Phys. Lett. B* **372** (1996) 271 [[hep-ph/9512339](#)].
- [102] R.S. Chivukula, B.A. Dobrescu, H. Georgi and C.T. Hill, *Top Quark Seesaw Theory of Electroweak Symmetry Breaking*, *Phys. Rev. D* **59** (1999) 075003 [[hep-ph/9809470](#)].
- [103] J. Chang, K. Cheung, J.S. Lee and C.-T. Lu, *Probing the Top-Yukawa Coupling in Associated Higgs production with a Single Top Quark*, *JHEP* **05** (2014) 062 [[1403.2053](#)].
- [104] CMS collaboration, *Search for the associated production of a Higgs boson with a single top quark in proton-proton collisions at $\sqrt{s} = 8$ TeV*, *JHEP* **06** (2016) 177 [[1509.08159](#)].
- [105] CMS collaboration, *Search for lepton flavour violating decays of the Higgs boson to $\mu\tau$ and $e\tau$ in proton-proton collisions at $\sqrt{s} = 13$ TeV*, *JHEP* **06** (2018) 001 [[1712.07173](#)].
- [106] CMS collaboration, *Search for $t\bar{t}H$ production in the $H \rightarrow b\bar{b}$ decay channel with leptonic $t\bar{t}$ decays in proton-proton collisions at $\sqrt{s} = 13$ TeV*, *JHEP* **03** (2019) 026 [[1804.03682](#)].
- [107] CMS collaboration, *Measurements of $t\bar{t}H$ Production and the CP Structure of the Yukawa Interaction between the Higgs Boson and Top Quark in the Diphoton Decay Channel*, *Phys. Rev. Lett.* **125** (2020) 061801 [[2003.10866](#)].
- [108] CMS collaboration, *Measurement of the Higgs boson production rate in association with top quarks in final states with electrons, muons, and hadronically decaying tau leptons at $\sqrt{s} = 13$ TeV*, *Eur. Phys. J. C* **81** (2021) 378 [[2011.03652](#)].
- [109] ATLAS collaboration, *Search for $H \rightarrow \gamma\gamma$ produced in association with top quarks and constraints on the Yukawa coupling between the top quark and the Higgs boson using data taken at 7 TeV and 8 TeV with the ATLAS detector*, *Phys. Lett. B* **740** (2015) 222 [[1409.3122](#)].

- [110] ATLAS collaboration, *Search for the Standard Model Higgs boson produced in association with top quarks and decaying into $b\bar{b}$ in pp collisions at $\sqrt{s} = 8$ TeV with the ATLAS detector*, *Eur. Phys. J. C* **75** (2015) 349 [[1503.05066](#)].
- [111] ATLAS collaboration, *Search for the Standard Model Higgs boson decaying into $b\bar{b}$ produced in association with top quarks decaying hadronically in pp collisions at $\sqrt{s} = 8$ TeV with the ATLAS detector*, *JHEP* **05** (2016) 160 [[1604.03812](#)].
- [112] ATLAS collaboration, *Observation of Higgs boson production in association with a top quark pair at the LHC with the ATLAS detector*, *Phys. Lett. B* **784** (2018) 173 [[1806.00425](#)].
- [113] ATLAS collaboration, *Measurement of Higgs boson decay into b-quarks in associated production with a top-quark pair in pp collisions at $\sqrt{s} = 13$ TeV with the ATLAS detector*, *JHEP* **06** (2022) 097 [[2111.06712](#)].
- [114] ATLAS collaboration, *Measurements of Higgs boson production cross-sections in the $H \rightarrow \tau^+\tau^-$ decay channel in pp collisions at $\sqrt{s} = 13$ TeV with the ATLAS detector*, [2201.08269](#).
- [115] A. Dabelstein, W. Hollik, C. Junger, R.A. Jimenez and J. Sola, *Strong supersymmetric quantum effects on the top quark width*, *Nucl. Phys. B* **454** (1995) 75 [[hep-ph/9503398](#)].
- [116] J.-j. Cao, R.J. Oakes, F. Wang and J.M. Yang, *Supersymmetric effects in top quark decay into polarized W boson*, *Phys. Rev. D* **68** (2003) 054019 [[hep-ph/0306278](#)].
- [117] F. del Aguila, M. Perez-Victoria and J. Santiago, *Observable contributions of new exotic quarks to quark mixing*, *JHEP* **09** (2000) 011 [[hep-ph/0007316](#)].
- [118] A. Belyaev, C.-R. Chen, K. Tobe and C.P. Yuan, *Phenomenology of littlest Higgs model with T^- parity: including effects of T^- odd fermions*, *Phys. Rev. D* **74** (2006) 115020 [[hep-ph/0609179](#)].
- [119] R. Contino, T. Kramer, M. Son and R. Sundrum, *Warped/composite phenomenology simplified*, *JHEP* **05** (2007) 074 [[hep-ph/0612180](#)].
- [120] J.A. Aguilar-Saavedra, *Identifying top partners at LHC*, *JHEP* **11** (2009) 030 [[0907.3155](#)].
- [121] Q.-H. Cao, Z. Li, J.-H. Yu and C.P. Yuan, *Discovery and Identification of W' and Z' in $SU(2) \times SU(2) \times U(1)$ Models at the LHC*, *Phys. Rev. D* **86** (2012) 095010 [[1205.3769](#)].
- [122] M. Farina, C. Grojean, F. Maltoni, E. Salvioni and A. Thamm, *Lifting degeneracies in Higgs couplings using single top production in association with a Higgs boson*, *JHEP* **05** (2013) 022 [[1211.3736](#)].
- [123] ALEPH, DELPHI, L3, OPAL, SLD, LEP ELECTROWEAK WORKING GROUP, SLD ELECTROWEAK GROUP, SLD HEAVY FLAVOUR GROUP collaboration, *Precision electroweak measurements on the Z resonance*, *Phys. Rept.* **427** (2006) 257 [[hep-ex/0509008](#)].
- [124] D. Barducci et al., *Interpreting top-quark LHC measurements in the standard-model effective field theory*, [1802.07237](#).

- [125] G. D’Ambrosio, G.F. Giudice, G. Isidori and A. Strumia, *Minimal flavor violation: An Effective field theory approach*, *Nucl. Phys. B* **645** (2002) 155 [[hep-ph/0207036](#)].
- [126] C. Degrande, G. Durieux, F. Maltoni, K. Mimasu, E. Vryonidou and C. Zhang, *Automated one-loop computations in the standard model effective field theory*, *Phys. Rev. D* **103** (2021) 096024 [[2008.11743](#)].
- [127] CMS collaboration, *Search for associated production of a Higgs boson and a single top quark in proton-proton collisions at $\sqrt{s} = 13$ TeV*, *Phys. Rev. D* **99** (2019) 092005 [[1811.09696](#)].
- [128] CMS collaboration, *Measurements of production cross sections of the Higgs boson in the four-lepton final state in proton-proton collisions at $\sqrt{s} = 13$ TeV*, *Eur. Phys. J. C* **81** (2021) 488 [[2103.04956](#)].
- [129] CMS collaboration, *Inclusive and differential cross section measurements of single top quark production in association with a Z boson in proton-proton collisions at $\sqrt{s} = 13$ TeV*, [2111.02860](#).
- [130] CMS collaboration, *Observation of tW production in the single-lepton channel in pp collisions at $\sqrt{s} = 13$ TeV*, *JHEP* **11** (2021) 111 [[2109.01706](#)].
- [131] ATLAS collaboration, *Measurements of the inclusive and differential production cross sections of a top-quark-antiquark pair in association with a Z boson at $\sqrt{s} = 13$ TeV with the ATLAS detector*, *Eur. Phys. J. C* **81** (2021) 737 [[2103.12603](#)].
- [132] ATLAS collaboration, *Combined measurements of Higgs boson production and decay using up to 139 fb^{-1} of proton-proton collision data at $\sqrt{s} = 13$ TeV collected with the ATLAS experiment*, .
- [133] ATLAS collaboration, *Combined effective field theory interpretation of Higgs boson and weak boson production and decay with ATLAS data and electroweak precision observables*, .
- [134] CMS collaboration, *Evidence for associated production of a Higgs boson with a top quark pair in final states with electrons, muons, and hadronically decaying τ leptons at $\sqrt{s} = 13$ TeV*, *JHEP* **08** (2018) 066 [[1803.05485](#)].
- [135] CMS collaboration, *Search for new physics using effective field theory in 13 TeV pp collision events that contain a top quark pair and a boosted Z or Higgs boson*, [2208.12837](#).
- [136] J. Brehmer, K. Cranmer, F. Kling and T. Plehn, *Better Higgs boson measurements through information geometry*, *Phys. Rev. D* **95** (2017) 073002 [[1612.05261](#)].
- [137] J. Alwall, R. Frederix, S. Frixione, V. Hirschi, F. Maltoni, O. Mattelaer et al., *The automated computation of tree-level and next-to-leading order differential cross sections, and their matching to parton shower simulations*, *JHEP* **07** (2014) 079 [[1405.0301](#)].
- [138] R.D. Ball, L. Del Debbio, S. Forte, A. Guffanti, J.I. Latorre, J. Rojo et al., *A first unbiased global NLO determination of parton distributions and their uncertainties*, *Nucl. Phys.* **B838** (2010) 136 [[1002.4407](#)].
- [139] LHC HIGGS CROSS SECTION WORKING GROUP collaboration, *Handbook of LHC Higgs Cross Sections: 4. Deciphering the Nature of the Higgs Sector*, [1610.07922](#).

- [140] ATLAS collaboration, *Measurements of Higgs boson production by gluon–gluon fusion and vector-boson fusion using $H \rightarrow WW^* \rightarrow e\nu\mu\nu$ decays in pp collisions at $\sqrt{s} = 13$ TeV with the ATLAS detector*, [2207.00338](#).
- [141] ATLAS collaboration, *Measurements of Higgs bosons decaying to bottom quarks from vector boson fusion production with the ATLAS experiment at $\sqrt{s} = 13$ TeV*, *Eur. Phys. J. C* **81** (2021) 537 [[2011.08280](#)].
- [142] ATLAS collaboration, *Measurement of the Higgs boson production cross section in association with a vector boson and decaying into WW^* with the ATLAS detector at $\sqrt{s} = 13$ TeV*, .
- [143] CMS collaboration, *Measurements of the Higgs boson production cross section and couplings in the W boson pair decay channel in proton-proton collisions at $\sqrt{s} = 13$ TeV*, [2206.09466](#).
- [144] CMS collaboration, *Measurements of Higgs boson production cross sections and couplings in the diphoton decay channel at $\sqrt{s} = 13$ TeV*, *JHEP* **07** (2021) 027 [[2103.06956](#)].
- [145] CMS collaboration, *Measurements of Higgs boson production in the decay channel with a pair of τ leptons in proton-proton collisions at $\sqrt{s} = 13$ TeV*, [2204.12957](#).
- [146] CMS collaboration, *Measurement of the single top quark and antiquark production cross sections in the t channel and their ratio in proton-proton collisions at $\sqrt{s} = 13$ TeV*, *Phys. Lett. B* **800** (2020) 135042 [[1812.10514](#)].
- [147] CMS collaboration, *Measurement of the differential cross section for t -channel single-top-quark production at $\sqrt{s} = 13$ TeV*, .
- [148] CMS collaboration, *Measurement of differential cross sections and charge ratios for t -channel single top quark production in proton–proton collisions at $\sqrt{s} = 13$ TeV*, *Eur. Phys. J. C* **80** (2020) 370 [[1907.08330](#)].
- [149] ATLAS collaboration, *Measurement of the inclusive cross-sections of single top-quark and top-antiquark t -channel production in pp collisions at $\sqrt{s} = 13$ TeV with the ATLAS detector*, *JHEP* **04** (2017) 086 [[1609.03920](#)].
- [150] CMS collaboration, *Measurement of differential cross sections for the production of top quark pairs and of additional jets in pp collisions at $\sqrt{s} = 13$ TeV*, .
- [151] ATLAS collaboration, *Inclusive and differential measurement of the charge asymmetry in $t\bar{t}$ events at 13 TeV with the ATLAS detector*, .
- [152] CMS collaboration, *Measurement of the $t\bar{t}$ charge asymmetry in events with highly Lorentz-boosted top quarks in pp collisions at $\sqrt{s} = 13$ TeV*, [2208.02751](#).
- [153] CMS collaboration, *Measurement of the cross section for top quark pair production in association with a W or Z boson in proton-proton collisions at $\sqrt{s} = 13$ TeV*, *JHEP* **08** (2018) 011 [[1711.02547](#)].
- [154] CMS collaboration, *Measurement of the production cross section for single top quarks in association with W bosons in proton-proton collisions at $\sqrt{s} = 13$ TeV*, *JHEP* **10** (2018) 117 [[1805.07399](#)].

- [155] ATLAS collaboration, *Observation of the associated production of a top quark and a Z boson in pp collisions at $\sqrt{s} = 13$ TeV with the ATLAS detector*, *JHEP* **07** (2020) 124 [[2002.07546](#)].
- [156] ATLAS collaboration, *Measurement of the cross-section for producing a W boson in association with a single top quark in pp collisions at $\sqrt{s} = 13$ TeV with ATLAS*, *JHEP* **01** (2018) 063 [[1612.07231](#)].
- [157] C.R. Rao, *Information and the accuracy attainable in the estimation of statistical parameters*, in *Breakthroughs in Statistics: Foundations and Basic Theory*, S. Kotz and N.L. Johnson, eds., (New York, NY), pp. 235–247, Springer New York (1992), [DOI](#).
- [158] F. James, *MINUIT Function Minimization and Error Analysis: Reference Manual Version 94.1*, .
- [159] F. Maltoni, L. Mantani and K. Mimasu, *Top-quark electroweak interactions at high energy*, *JHEP* **10** (2019) 004 [[1904.05637](#)].
- [160] H.E. Faham, *tWZ production at NLO in QCD in the SMEFT*, in *14th International Workshop on Top Quark Physics*, 12, 2021 [[2112.13282](#)].
- [161] T. Sjostrand, S. Mrenna and P.Z. Skands, *PYTHIA 6.4 Physics and Manual*, *JHEP* **05** (2006) 026 [[hep-ph/0603175](#)].
- [162] T. Sjostrand, S. Mrenna and P.Z. Skands, *A Brief Introduction to PYTHIA 8.1*, *Comput. Phys. Commun.* **178** (2008) 852 [[0710.3820](#)].
- [163] DELPHES 3 collaboration, *DELPHES 3, A modular framework for fast simulation of a generic collider experiment*, *JHEP* **02** (2014) 057 [[1307.6346](#)].
- [164] V. Hirschi and O. Mattelaer, *Automated event generation for loop-induced processes*, *JHEP* **10** (2015) 146 [[1507.00020](#)].
- [165] M. Cacciari, G.P. Salam and G. Soyez, *FastJet User Manual*, *Eur. Phys. J.* **C72** (2012) 1896 [[1111.6097](#)].
- [166] Y.L. Dokshitzer, G.D. Leder, S. Moretti and B.R. Webber, *Better jet clustering algorithms*, *JHEP* **08** (1997) 001 [[hep-ph/9707323](#)].
- [167] J.M. Butterworth, A.R. Davison, M. Rubin and G.P. Salam, *Jet substructure as a new Higgs search channel at the LHC*, *Phys. Rev. Lett.* **100** (2008) 242001 [[0802.2470](#)].
- [168] M. Dasgupta, A. Fregoso, S. Marzani and G.P. Salam, *Towards an understanding of jet substructure*, *JHEP* **09** (2013) 029 [[1307.0007](#)].
- [169] T. Plehn, M. Spannowsky, M. Takeuchi and D. Zerwas, *Stop Reconstruction with Tagged Tops*, *JHEP* **10** (2010) 078 [[1006.2833](#)].
- [170] G. Kasieczka, T. Plehn, T. Schell, T. Strebler and G.P. Salam, *Resonance Searches with an Updated Top Tagger*, *JHEP* **06** (2015) 203 [[1503.05921](#)].
- [171] CMS collaboration, *Search for supersymmetry in pp collisions at $\sqrt{s} = 13$ TeV in the single-lepton final state using the sum of masses of large-radius jets*, *JHEP* **08** (2016) 122 [[1605.04608](#)].